PENNSTATE

1855

PROPULSION ENGINEERING RESEARCH CENTER

Combustion of Lox with $H_{2(g)}$ Under Subcritical, Critical, and Supercritical Conditions (Task 1)
and
Experimental Observation of Dense Spray and Mixing of Impinging Jets (Task 2)

ANNUAL REPORT

SUBMITTED BY: K.K.Kuo, W.H.Hsieh and F.B.Cheung

TO
Mr. Klaus W. Gross, Code: EP 55
NASA Marshall Space Flight Center
Huntsville, Alabama 35812

A UNIVERSITY SPACE ENGINEERING RESEARCH CENTER

106 RESEARCH BUILDING EAST
UNIVERSITY PARK, PENNSYLVANIA 16801

ANNUAL REPORT

COMBUSTION OF LOX WITH $H_{2(g)}$ UNDER SUBCRITICAL, CRITICAL, AND SUPERCRITICAL CONDITIONS (Task 1)

and

EXPERIMENTAL OBSERVATION OF DENSE SPRAY AND MIXING OF IMPINGING JETS (Task 2)

Submitted to

Mr. Klaus W. Gross
Code:EP 55
NASA: Marshall Space Flight Center
Huntsville, Alabama 35812

Prepared by

K. K. Kuo, W. H. Hsieh, A. S. Yang and J. J. Brown (Task 1)

K. K. Kuo, F. B. Cheung, R. D. Woodward,
M. C. Kline and R. L. Burch (for Task 2)

PROPULSION ENGINEERING RESEARCH CENTER
The Pennsylvania State University
University Park, PA 16802

February 28, 1992

TABLE OF CONTENTS

TASK NO. 1 COMBUSTION OF LOX WITH $H_{2(g)}$ UNDER SUBCRITICAL, CRITICAL, AND SUPERCRITICAL CONDITIONS

TABLE OF CONTENTS (Cont'd)

TASK NO 2: EXPERIMENTAL OBSERVATION OF DENSE SPRAY AND MIXING OF IMPINGING JETS

ACKNOWLEDGMENT

This research project has been funded by NASA-MSFC under Contract Number NAG8-174. The authors would like to thank Mr. Klaus W. Gross of MSFC for his encouragement and support. A part of this work was supported by the Space Propulsion Engineering Center at The Pennsylvania State University (PSU). The interest and support of Prof. Charles L. Merkle, Director of SPEC, is also acknowledged. Valuable input from Mr. David T. Harrje, a specialist in liquid rocket propulsion, on supercritical combusiton of LOX is deeply acknowledged. The support of AFRAP fellowship from AFOSR for Mr. Robert Burch to participate on this project is also appreciated.

LIST OF FIGURES

NOMENCLATURE

$a,\ b$	= Constant in Redlich-Kwong equation of state
C_p	= Constant-pressure specific heat
D_{im}	= Effective mass diffusivity of species i
D_{ij}	= Binary mass diffusivity
E_H	= Activation energy
f	= Fugacity
h	= Enthalpy
h_f^o	= Heat of formation
ΔH_v	= Latent heat of vaporization
$L_g,\ L_l$	= Length for the gas- and liquid-phase regions
$\dot{m}''$	= Mass consumption rate per unit surface area of LOX
N	= Total number of species
n_i	= Number of moles of species i
P	= Pressure
$R_I,\ R_O$	= Inner and outer radius for the gas-phase region
R_u	= Universal gas constant
r	= Coordinate in the transverse direction
r_l	= Feeding velocity of LOX
T	= Temperature
$u,\ v$	= Velocity in x and r direction
V	= Total volume
$\vec{V}$	= Velocity vector
W	= Molecular weight
x	= Coordinate in the axial direction
X	= Mole fraction
Y	= Mass fraction
Z	= Compressibility factor
Z_H	= Reaction rate constant

Greek Symbols

λ = Thermal conductivity

μ = Viscosity

ρ = Density

$\dot{\omega}$ = Rate of production

Superscripts

$(\ )^{(l)}$ = Liquid phase

$(\ )^{o}$ = Ideal state

$(\ )^{(v)}$ = Vapor phase

$(\bar{\ })$ = Partial molar quantity

Subscripts

$(\ )_i$ = Species i

$(\ )_o$ = Gas-phase inlet conditions of surrounding purge flows

$(\ )_s$ = Surface value

$(\ )_+$, $(\ )_-$ = Interfacial conditions on the gas and liquid sides

Task No. 1

COMBUSTION OF LOX WITH $H_{2(g)}$ UNDER SUBCRITICAL, CRITICAL, AND SUPERCRITICAL CONDITIONS

K. K. Kuo, W. H. Hsieh, A. S. Yang, and J. J. Brown
Propulsion Engineering Research Center
The Pennsylvania State University
University Park, PA 16802

1. INTRODUCTION

This annual report summarizes the progress made during the period of February 1, 1991 to January 31, 1992, under Task 1 of the contract entitled "Combustion of LOX with $H_{2(g)}$ under Subcritical, Critical, and Supercritical Conditions."

The general objective of this investigation is to achieve a better understanding of the combustion processes of liquid oxygen and gaseous hydrogen under broad range of pressure covering subcritical, critical, and supercritical conditions. Specific objectives of the research program are:

1. To determine the evaporation- and burning-rate characteristics of LOX in $H_{2(g)}/N_{2(g)}$ environment under broad ranges of operating conditions;
2. To observe the change in the density gradient of the flame zone using the Schlieren flow visualization method;
3. To inspect regions with high water vapor concentration, which indicates the active reaction zone of oxygen with hydrogen, adopting laser light-sheet technique;
4. To measure species concentration profiles and surface temperature of LOX employing the gas chromatography and fine-wire thermocouples, respectively;
5. To examine the validity of high-pressure vapor-liquid equilibria at the liquid surface of LOX;
6. To formulate and solve a theoretical model for simulating the two-phase evaporation and combustion processes of LOX with hydrogen/nitrogen; and
7. To validate the theoretical model with the measured experimental data.

2. EXPERIMENTAL APPROACH

The scope of the experimental work performed during this reporting period falls into the following areas: (1) design of the overall experimental setup; (2) modification of an existing windowed high-pressure chamber; (3) design of the LOX feeding system; (4) provision of the safety features in the test rig design; (5) LOX cleanliness requirements; (6) cold shock testing; (7) implementation of data acquisition system; (8) preliminary tests for system check-out (9)modification of LOX feeding system; and (10) evaporation tests. The progress made in each subject area is discussed below.

2.1 Design of the Overall Experimental Setup

A layout of the experimental setup for studying the evaporation and combustion characteristics of LOX with gaseous hydrogen under broad ranges of operating conditions is shown in Fig. 1.1. A picture of the assembled LOX testing facility is also given in Fig. 1.2. The liquid surface of LOX is kept at a fixed location by a LOX level control system described in Sec. 2.3.

A computer-controlled $H_{2(g)}/N_{2(g)}$ gas supply system has been incorporated into the setup to maintain the chamber pressure at a prespecified level. In order to accurately measure mass fractions of hydrogen and nitrogen in the mixture, two electronic mass flowmeters have been adopted because of the following unique properties: (1) it measures mass flowrate directly; (2) the maximum pressure rating is up to 1500 psig; (3) the flowrate range is broad (from 0 to 100 SLM); (4) the accuracy is $\pm 2\%$ full scale; (5) the repeatability is $\pm 0.2\%$ full scale; and (6) the response time is 1.2 sec. Most components of the experimental setup have been assembled in a mobile test stand, which provides the capability of moving the experimental setup to test sites where various diagnostic instruments are located.

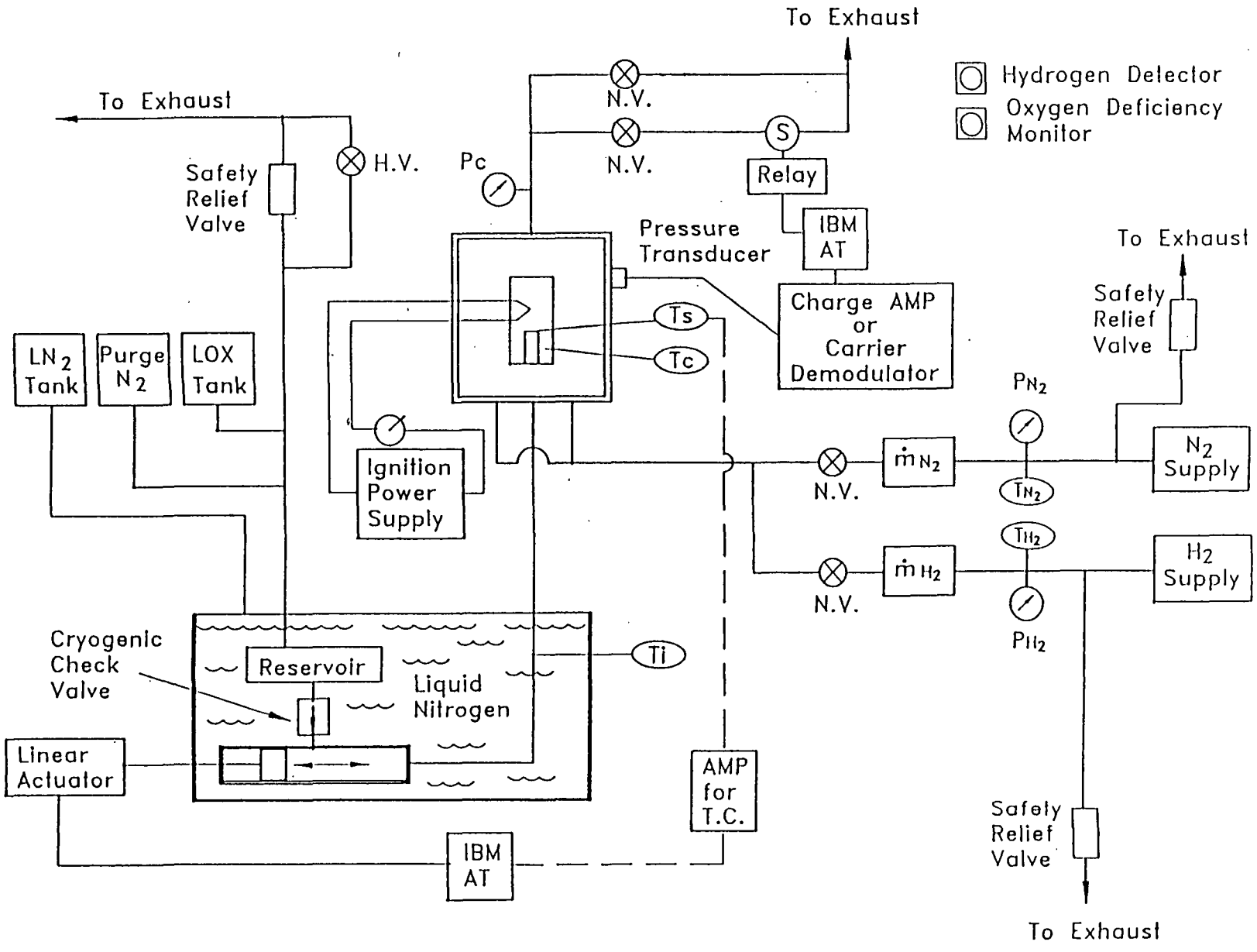

Fig. 1.1 Layout of the Overall Experimental Setup

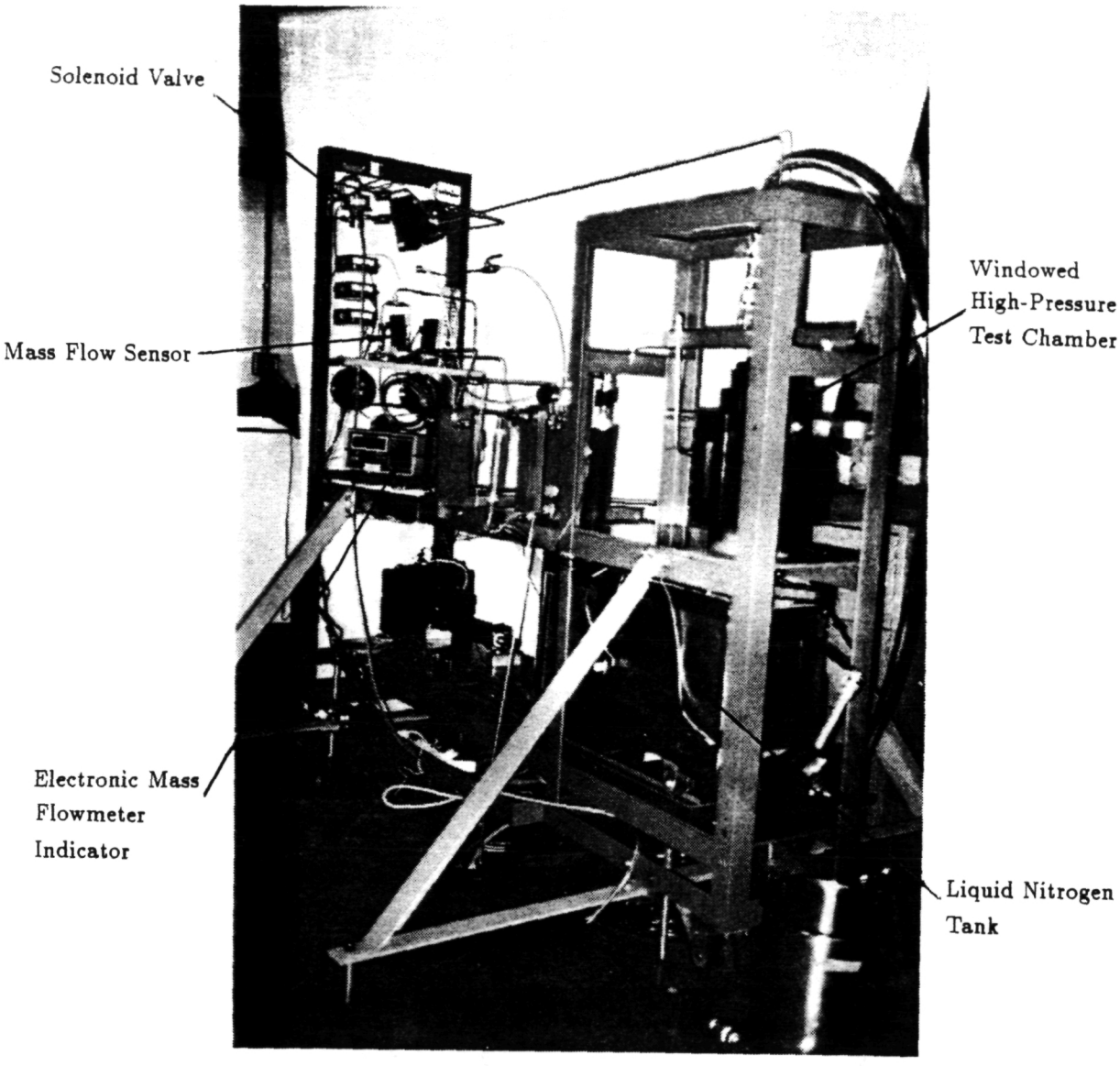

Fig. 1.2 Picture of the Assembled LOX Testing Facility

2.2 Modification of the Existing Windowed High-Pressure Combustor

An existing windowed high-pressure combustor has been modified to study the $LOX/H_{2(g)}$ combustion phenomena. Figure 1.3 is a picture showing the front view of the modified combustor. The bottom piece assembly including the internal assembly holder, bottom piece retainer, and sintered porous base plate were designed and manufactured during this reporting period, and other components are from an existing combustor.

The air gap formed by the concentric tubes at the middle port of the bottom piece serves as a thermal insulator to reduce the rate of heat transfer from the combustor to oxygen and keep oxygen in the liquid state. In the internal assembly holder, four of the six annular ports are provided for thermocouples, which are adopted to measure the chamber temperature and the LOX surface temperature at the top end of the feeding tube. The remaining two ports are used as the inlets of the hydrogen/nitrogen flow. The bottom piece is constructed with an 80-micron (maximum particle stoppage) sintered stainless-steel plate to uniformize the incoming $H_{2(g)}/N_{2(g)}$ flow around the LOX feeding tube and to smooth out sudden pressure fluctuations at the upstream to avoid combustion instabilities during firing tests.

2.3 Design of the LOX Feeding System

Figure 1.4 shows a schematic diagram of the LOX feeding system of our initial design, which was modified due to the leakage problem associated with a positive displacement feeder system. The modified LOX feeding system is given in Sec. 2.9. The system configuration was designed in such a manner that almost all LOX-related parts were immersed in liquid nitrogen bath to minimize the evaporation of liquid oxygen, and thereby maintaining oxygen in its liquid state throughout the feeding line. (Detailed design drawings of the liquid nitrogen tank is given in Fig. 1.5.) During the oxygen filling process, the liquid oxygen was first transported

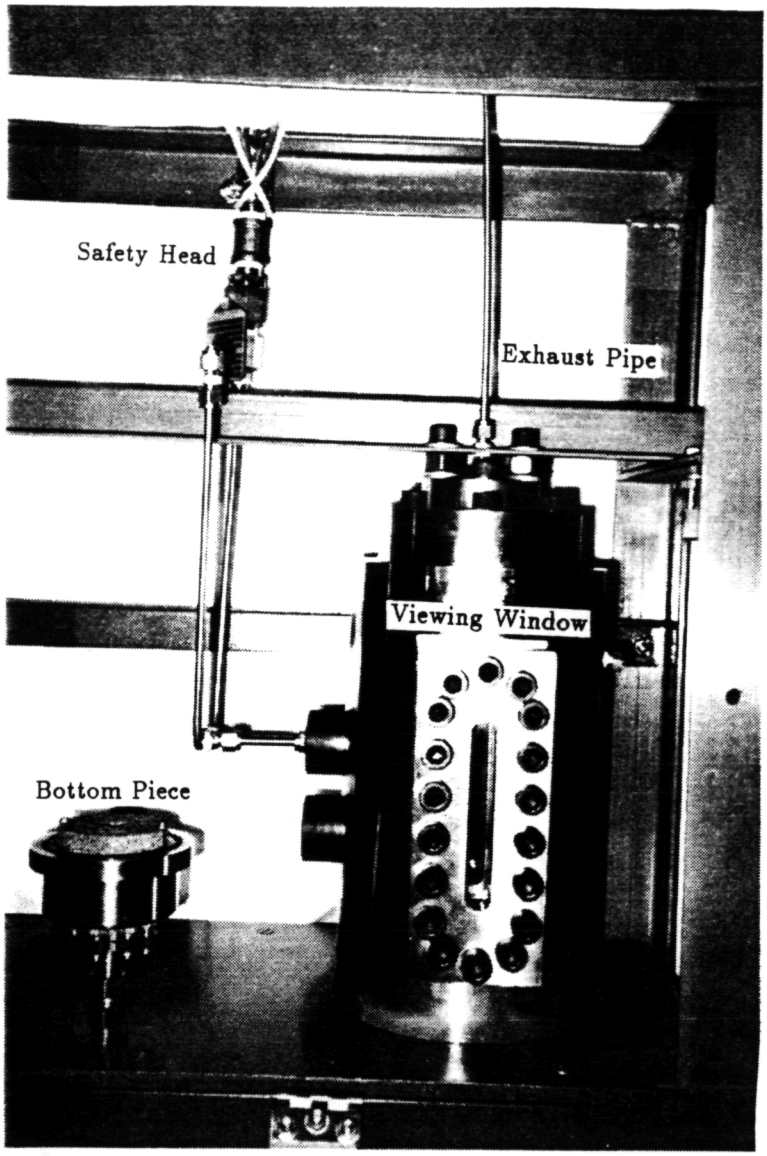

Fig. 1.3 Front View of the Modified Combustor

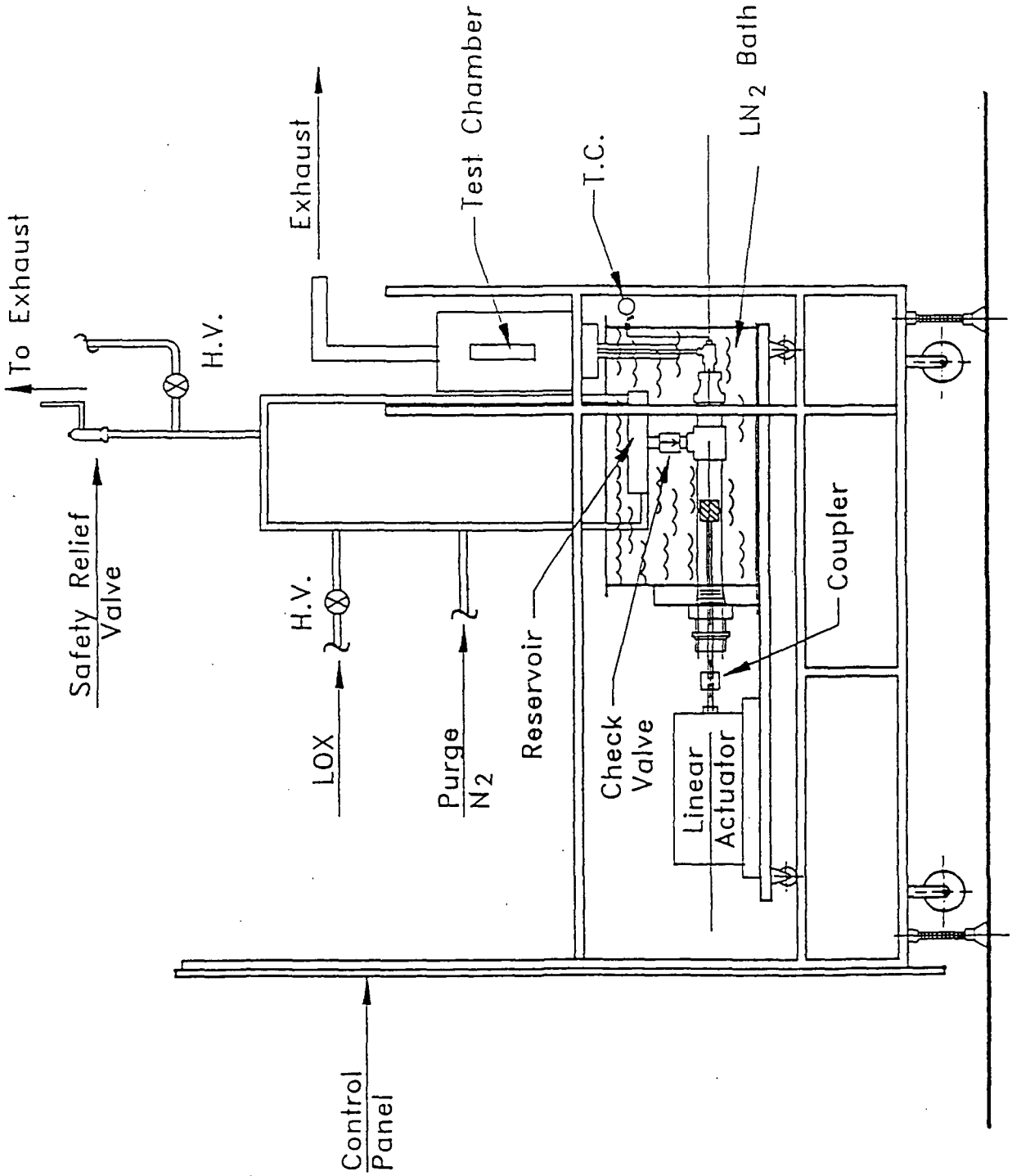

Fig. 1.4 Schematic Diagram of the LOX Feeding System

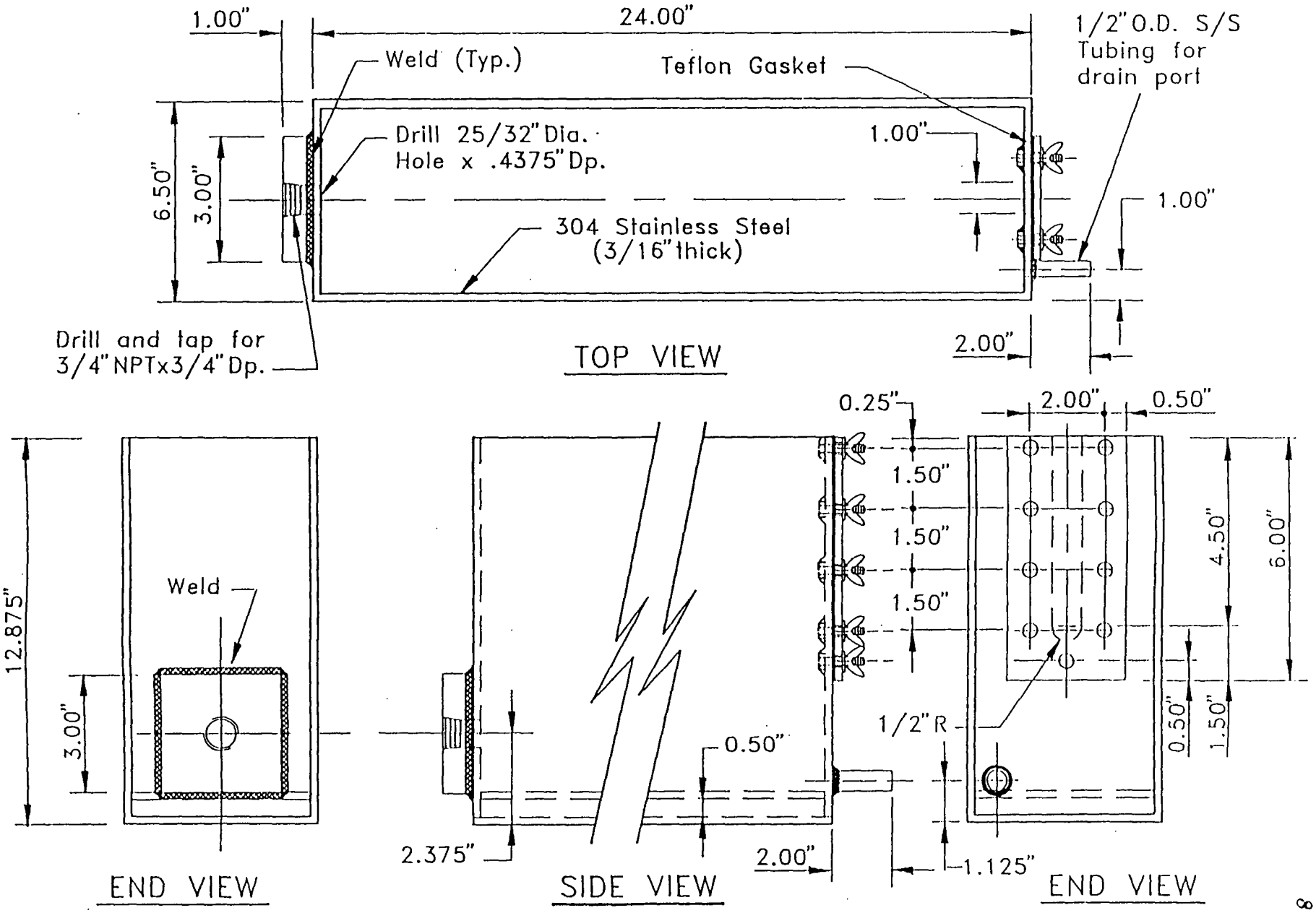

Fig. 1.5 Liquid Nitrogen Tank Design

from a LOX dewar and stored in a reservoir. Here the reservoir served as a phase separator, and the gaseous oxygen could be discharged through a vent line. When two hand valves were closed, the liquid oxygen driven by the oxygen vapor pressure could pass through a cryogenic check valve (8.0 psi cracking pressure) and flow into the feeding cylinder. Meanwhile, the piston was designed to retracted slowly to achieve a smooth inflow process and prevent the formation of bubbles inside the cylinder.

Figure 1.6 exhibits the initial design of the LOX feeding cylinder and piston. A spring-loaded type seal (see Fig. 1.7) was adopted due to its low load, high deflection spring, which was supposed to provide low friction sealing and compensate for any minor hardware misalignment. A separate back-up ring arrangement was included in this dynamic sealing design to avoid serious extrusion under high-pressure conditions. Carbon/graphite filled PTFE was selected as the seal material to avoid the use of any lubricant, which could cause contamination of the system. The concept of split glands in piston applications was also utilized in the design of the piston head unit to eliminate stretching or compressing seals during installation.

An IDC S21205B linear actuator with its SAX controller was employed in this study. The features of this S-series actuator and controller are: (1) resolution of 0.0005 inches; (2) rated life in excess of five million cycles; (3) thrust load carrying capabilities up to 800 pounds; and (4) integrated package including drive electronics, power supply, heat sink, and programmable motion controller. A LOX level control system consisted of the above-mentioned linear actuator, actuator controller, and a thermocouple for measuring the LOX temperature at the exit of the feeding. An analog-to-digital converter and an IBM/PC-AT computer were implemented in the early phase of the experimental setup. A computer program for interfacing and controlling the functions of various components was also implemented and tested.

In spite of the above detailed design of hardware and its control system, a major difficulty in piston leakage was encountered due to the improper function of

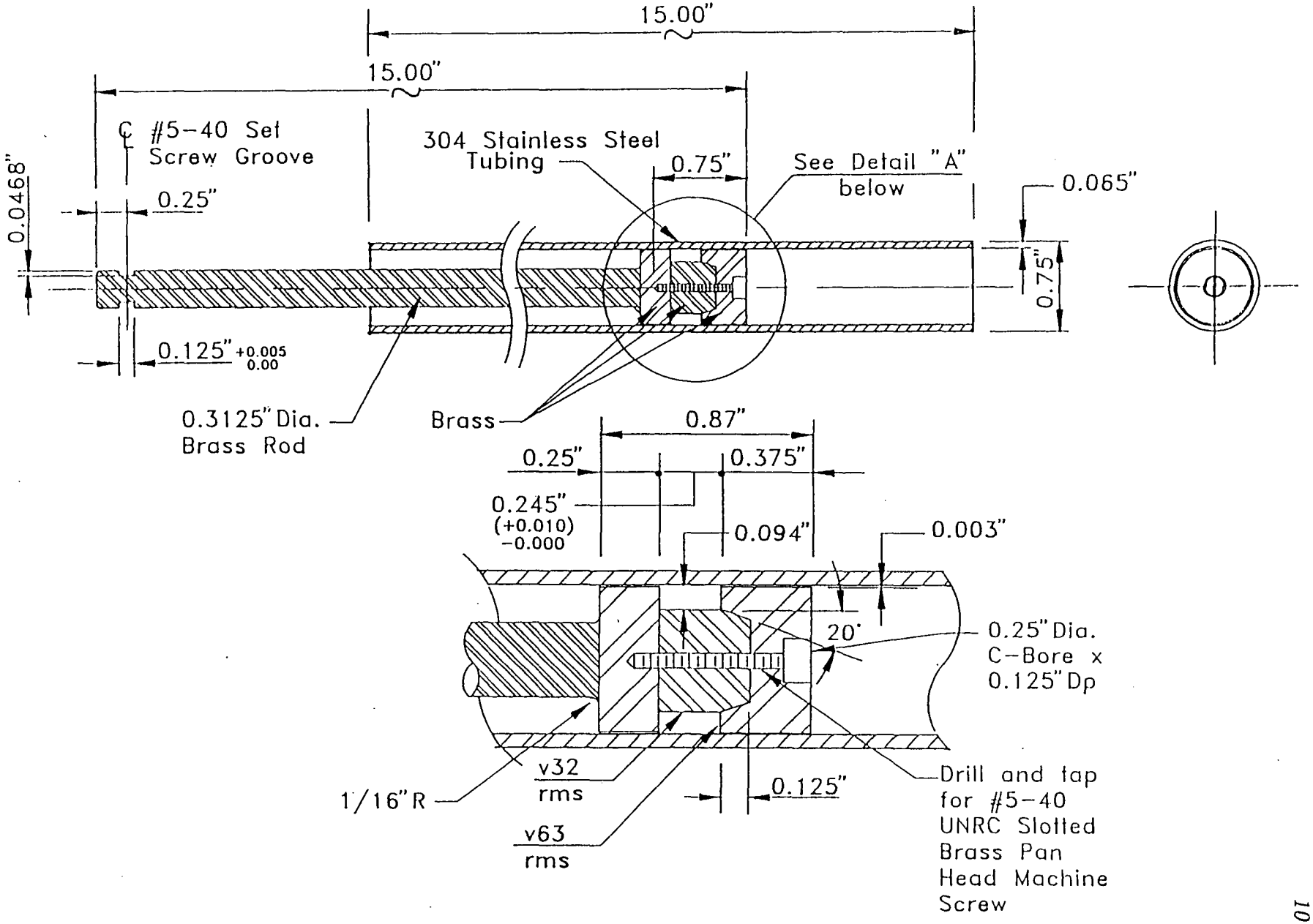

Fig. 1.6 Design of LOX Feeding Cylinder and Piston

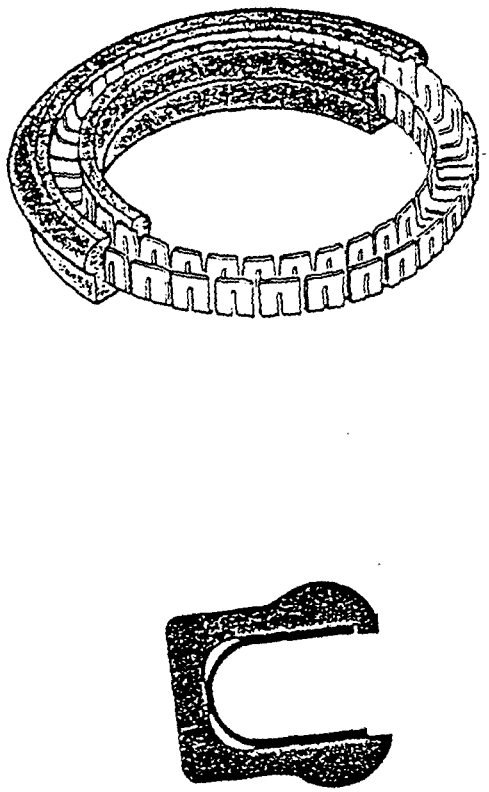

Fig. 1.7 Schematic Diagram of Spring-Loaded Type Seals

the spring loaded seal ring. Therefore, an alternative way for feeding and controlling LOX feeding was developed and discussed in Sec. 2.9. The piston feeding system can still be used for non-cryogenic fluids.

2.4 Safety Features in the Test Rig Design

The design and operation of systems involving hydrogen and oxygen have been in practice for a long time, but safety concerns should always be taken with special cautions. The wide flammability range and the low ignition energy of hydrogen necessitate special management of hydrogen to minimize possible fire hazards. A solid-state semiconductor-type hydrogen detector is installed for continuous, long-term operation to detect any hydrogen leakage. The threshold level of hydrogen for triggering an alarm signal of the detector is 300 ppm.

Although nitrogen gas from the evaporation of LN_2 is odorless and nontoxic, decreasing the oxygen content in the air can be caused by the evaporation of N_2 and lead to suffocation for personnel. An oxygen deficiency monitor has been employed to measure oxygen concentration in the air. When the O_2 concentration is below 19.5%, an audible alarm along with a visual warning LED will be activated.

In order to avoid the high-pressure gas induced ruptures of piping system or the trapping of liquid oxygen between closed valves, a low-pressure safety relief valve with adjustable cracking pressure from 0 to 225 psi has been implemented in the LOX supply line. As for both the hydrogen and nitrogen supply lines, two safety relief valves with adjustable pressure range of 750 - 1500 psi were mounted to protect electronic mass flowmeters and pressure gauges from over-pressurized conditions. Furthermore, a rupture disc with bursting pressure of 1450 psi has been adopted to prevent the test chamber from over-pressurization.

2.5 LOX Cleanliness Requirements

Contaminants such as machining oils, thread lubricants, and fine particles could burn violently in oxygen-enriched environments. Before being used, the LOX feeding system was degreased by washing with approved grease-removing solvents. After the completion of solvent cleaning, all gross residual cleaning fluid was drained. Subsequently, the components were purged and dried with warm, dry, oil-free compressed air or nitrogen. In this research work, a step-by-step cleaning procedure for components employed in gaseous or liquid oxygen service is given as follows.

1. Mix the detergent *MICRO*^{R} (from Cole-Parmen Company) with water to form a 2% cleaning fluid solution, and heat the solution to 66°C (150°F).
2. Soak the component in the solution and start ultrasonic agitation to remove any gross contaminants in a couple of hours depending upon the level of contamination and the size of component. (For example, it took one day to perform the precleaning work for the LOX reservoir.)
3. Drain the solution, rinse with water, and permit the component to dry.
4. Fully immerse the component in solvent 1,1,1-trichloroethane (from EM Science) to wet all internal surfaces for about 10 minutes. Ultrasonic cleaning is still activated when proceeding this step.
5. Remove the component and drain all gross cleaning fluid.
6. Rinse with dehydrated alcohol (200 proof) to eliminate any residue of solvent.
7. Blow dry with clean nitrogen, and
8. Use an ultraviolet light (with wave length between 254 and 366 nm) to inspect the presence of contamination. A lack of fluorescence indicates that cleaned surfaces are free of any hydrocarbon contaminants. If fluorescence shows up as a blotch, smear, smudge, or film, return to step 4. Several cycles may be required to achieve the acceptable degree of cleanliness.

2.6 Cold Shock Testing

It is well known that the expansion and contraction from the thermal cycling can impose excessive stresses on components for cryogenic services. In this work, the LOX feeding system consisting of components such as LOX reservoir, cryogenic check valve, LOX feeding cylinder and piston, and several Swagelok tube fittings has been cold-shock tested by means of being immersed in liquid nitrogen bath. The goal of cold shock conditioning is to examine the system integrity. After the LOX feeding system has been warmed to ambient temperature, attention was paid to inspect the parts for evidence of cracking, or distortion, and then all fittings and connectors were retorqued.

2.7 Implementation of Data Acquisition System

A DAS-8GPA data acquisition-and-control board was installed on a personal computer. A software for interfacing, multi-channel scanning, and controlling the operations of feeding and gas-supply processes was also completed and tested. In this investigation, one of the major task is to determine the pressure effect on the burning-rate characteristics and flame structure. The chamber pressure was measured by a Validyne pressure transducer (DP215) and a carrier demodulator (CD15) with a frequency of 1 KHZ. The pressure signal was continuously scanned and monitored by a computer. When the chamber pressure exceeds a prespecified value, a digital output will be activated immediately. Because the output signal from digital I/O port of DAS-8 board is not strong enough to drive the ON-OFF action of the solenoid valve, an electric circuit employing a key amplifier component (a linear J-FET input OP-AMP) was designed, fabricated, and tested to boost the current of signal without changing its voltage. A Skinner (two-way normally closed) solenoid valve with response time of 4-8 milliseconds was employed to maintain the chamber pressure at a preset level. Using the afore-mentioned apparatus, the

pressure fluctuation of the test chamber could be well limited within $\pm 1\%$ of preset pressure level (1 - 68 atm).

In addition, three sets of J-type temperature meter (OMEGA DP701) and thermocouple with measurement range of -204.0 to 900.0^{o}C were implemented to constantly display the inlet and surface temperatures of LOX.

2.8 Preliminary Tests for System Check-out

During this reporting period, the liquid nitrogen and various gas supply lines were accomplished. The function checkup of safety devices, including hydrogen detector(SMC, Model 2001) and oxygen deficiency monitor(SMC, model 55), was carried out. Two safety relief valves with setting values of 1250 psi were mounted respectively on nitrogen and hydrogen supply lines to protect electronic mass flow sensors and pressure gauges from over-pressurized situations. Several system check-out tests were conducted under one atmospheric condition for the LOX feeding system. Results showed that the original design of the LOX feeding cylinder and piston assembly failed to meet the sealing requirement. The reason is given as follows.

In cryogenic sealing, cold temperature liquids cause Teflon and other Furon sealing materials to shrink and harden. The spring loaded seal ring after shrinkage can not provide enough compression force against the cylinder wall. Under the very low temperature condition such as -197^{o}C (the condition of liquid nitrogen bath), even stainless steel spring became stiff and deteriorated its resilience. Thus, the leakage problem was present in the piston feeder system.

2.9 Modification of LOX Feeding System

To overcome the leakage problem, another cylinder/piston assembly, as shown in Figs. 1.8 and 1.9, was designed and fabricated. Two important features have been incorporated into the design consideration. First, multi-stage sealing:

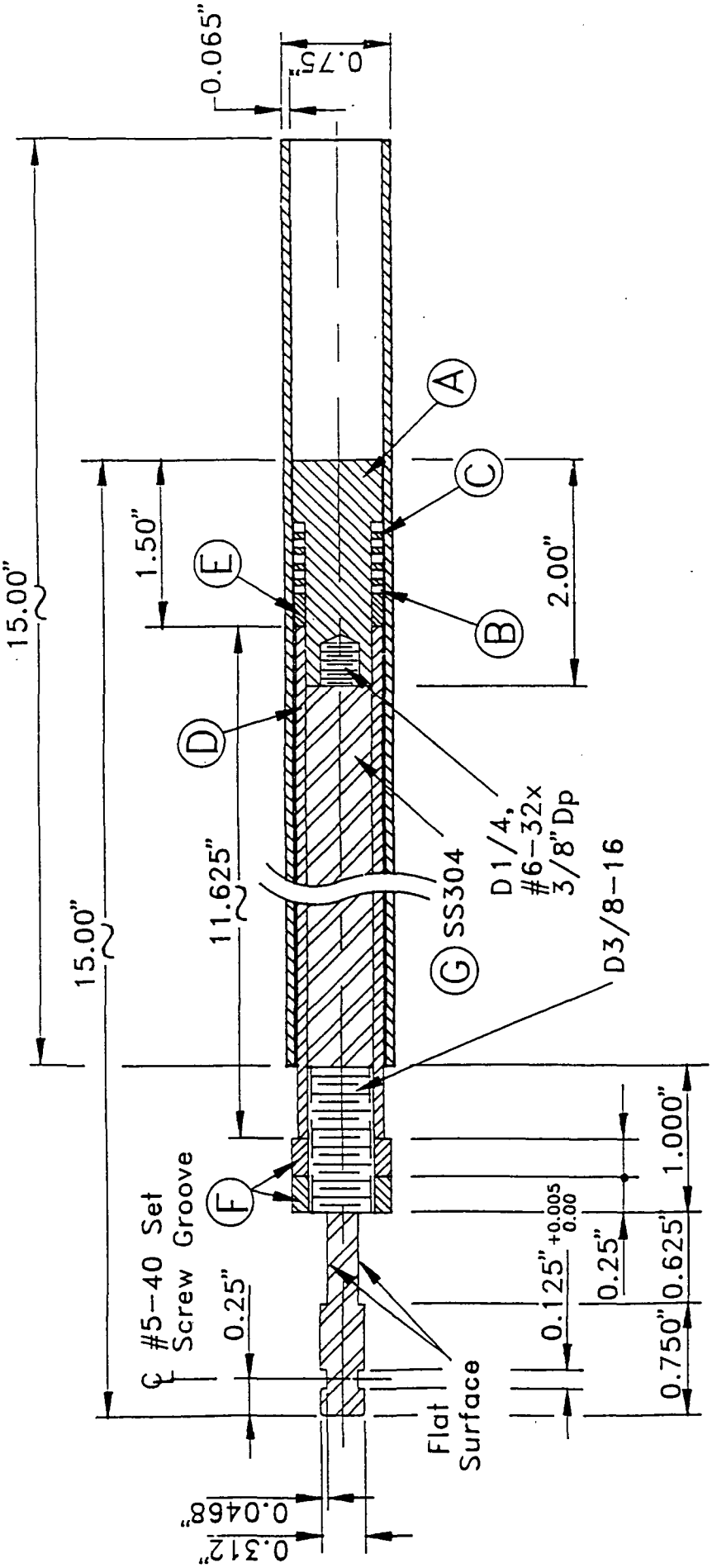

Fig. 1.8 Assembly of Multi-stage Cylinder/Piston Design

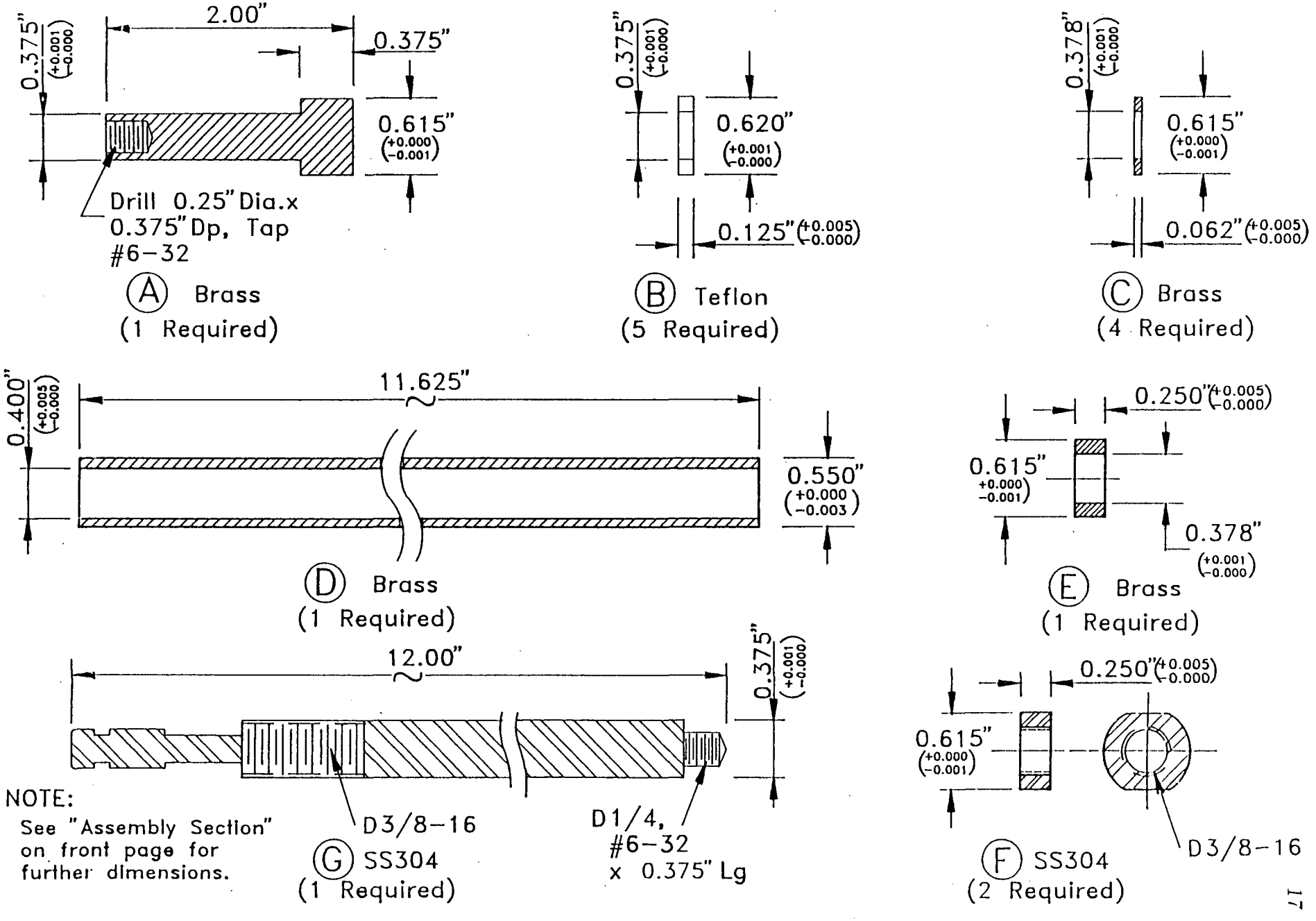

Fig. 1.9 Components of Multi-stage Cylinder/Piston Design

The relative reciprocating motion tends to slide or roll five Teflon rings back and forth to achieve sealing purpose. Second, Adjustable compression of the seal: The seals must be radially compressed between the bottom of the seal groove and the cylinder wall for proper sealing action. It was expected that Teflon material would seal at the extremely low temperature by increasing the compression force. The testing results of the multi-stage cylinder/piston design showed some improvement in the sealing ability. However, a small amount of leakage was still detected during the tests. Moreover, the nuts in the end of the piston rod need to be constantly re-tightened for increasing radial compression. This procedure shortens the service lifetime of seals. Moving seals may even fail because of serious abrasion against the cylinder wall. Owing to the above drawbacks, it is felt that the design of the cylinder/piston assembly is not suitable for operation in extremely low temperature, and must be modified based on the design principle of eliminating the moving parts in the LOX feeding system.

Figure 1.10 shows a modified arrangement of the overall experimental setup. Gaseous oxygen is delivered into the feeding cylinder immersed in the liquid nitrogen bath. Through the heat transfer, the oxygen is liquefied and eventually fill in the interior space of cylinder as a reservoir for LOX. By adjusting the opening of a micro-metering valve, the minimum LOX mass consumption rate, required to maintain a stable surface at the exit of the LOX feeding tube, can be achieved at a specified operating condition. This modified system has demonstrated successful operation by maintaining the LOX surface at the opening of the feeding tube.

2.10 Evaporation Tests

The assumption of the phase equilibrium at the gas/liquid interface is widely used in studying the gasification and burning of the droplet at near-critical and supercritical conditions. However, very limited experimental research has been carried out to justify this assumption, even though the high-pressure vapor-liquid

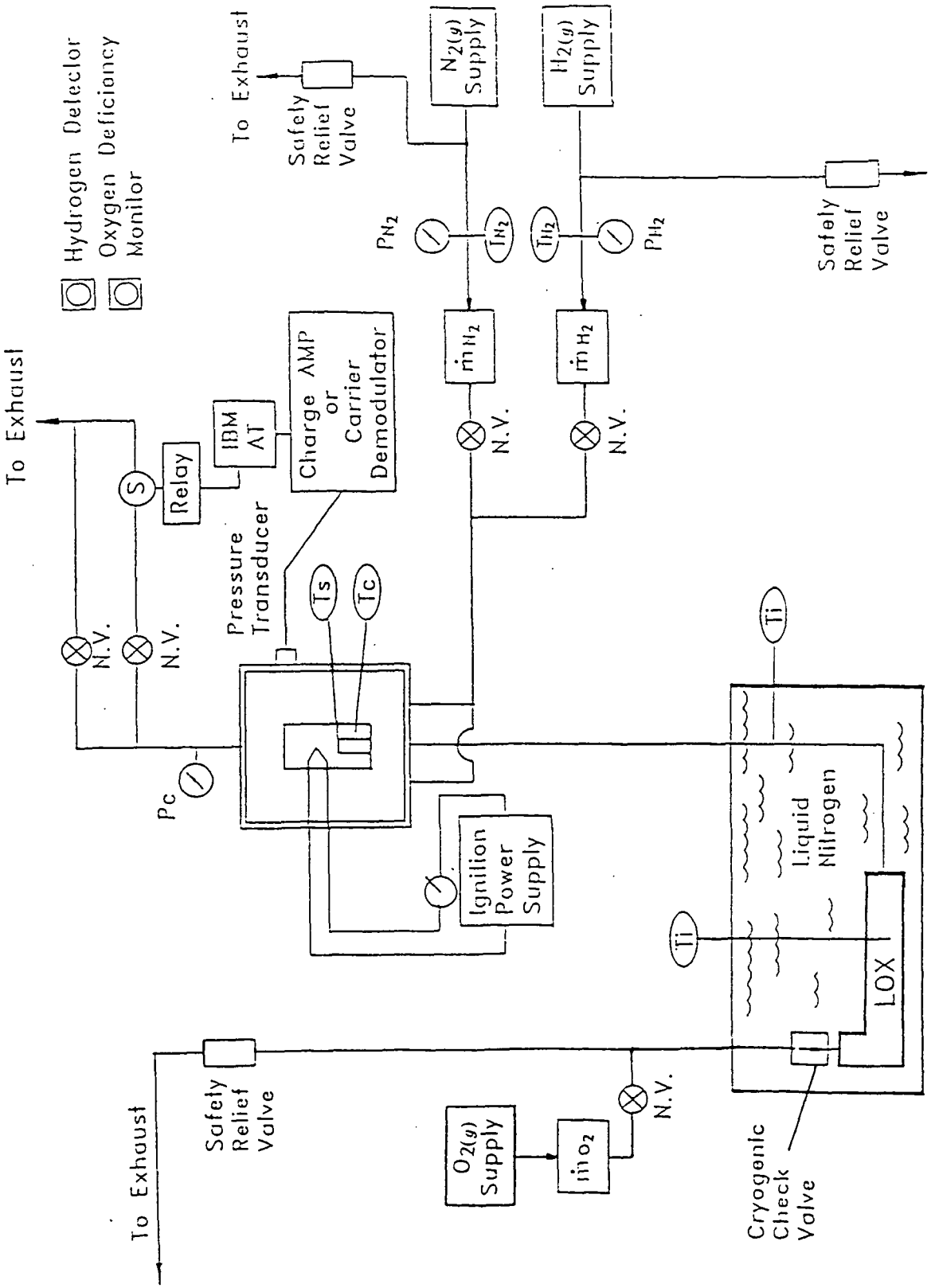

Fig. 1.10 Arrangement of the Modified Experimental Setup

equilibrium plays a decisive role in defining gas/liquid interfacial boundary conditions. In this work, a number of evaporation tests have been conducted to determine the pressure dependence on the evaporation rate and the surface temperature of LOX. The species concentrations in the gas phase are also measured using the gas chromatography. The experimental data could be used to examine the validity of enforcing high-pressure vapor-liquid equilibria on the liquid surface of LOX. The evaporation tests are now proceeding. For safety reasons, the test procedure was followed strictly in accordance with the operation manual (see Appendix A). A detailed discussion of testing results will be given in the next progress report.

3. THEORETICAL FORMULATION

A comprehensive model has been developed to study the two-phase evaporation and combustion characteristics of liquid oxygen with hydrogen/nitrogen mixture under subcritical, near critical and supercritical conditions. The model considers a column of LOX reacting with H_2/N_2 mixture as shown in Fig. 1.11. The tubes, through which the LOX and H_2/N_2 mixture flow, are concentric with radii R_I and R_O, respectively. Steady-state calculations are obtained by supplying the LOX at a certain feeding rate which can keep its surface stationary. The gaseous oxygen and hydrogen react and form a stable diffusion flame anchored at the exit of the inner tube. In the analysis, the gas and liquid phases are treated separately. They are then conjugated together through the use of the liquid-vapor phase equilibrium and the balances of mass and energy at the gas/liquid interfaces.

3.1 Gas-Phase Analysis

For the gas-phase analysis, the model consists of a set of conservation equations for mass, momentum, energy and species concentration in a multicomponent system with the consideration of ambient gas solubility, variable thermophysical properties, vanishing surface tension and latent heat of vaporization at critical mixing point, and chemical kinetics. Due to the large temperature difference between the LOX surface and the surrounding flow, the effect of gravitational body force on the x-momentum equation becomes significant and is taken into account. If viscous dissipation, Dufour and Soret effects, and radiative heat transfer are neglected, the governing equations can be written as shown below:

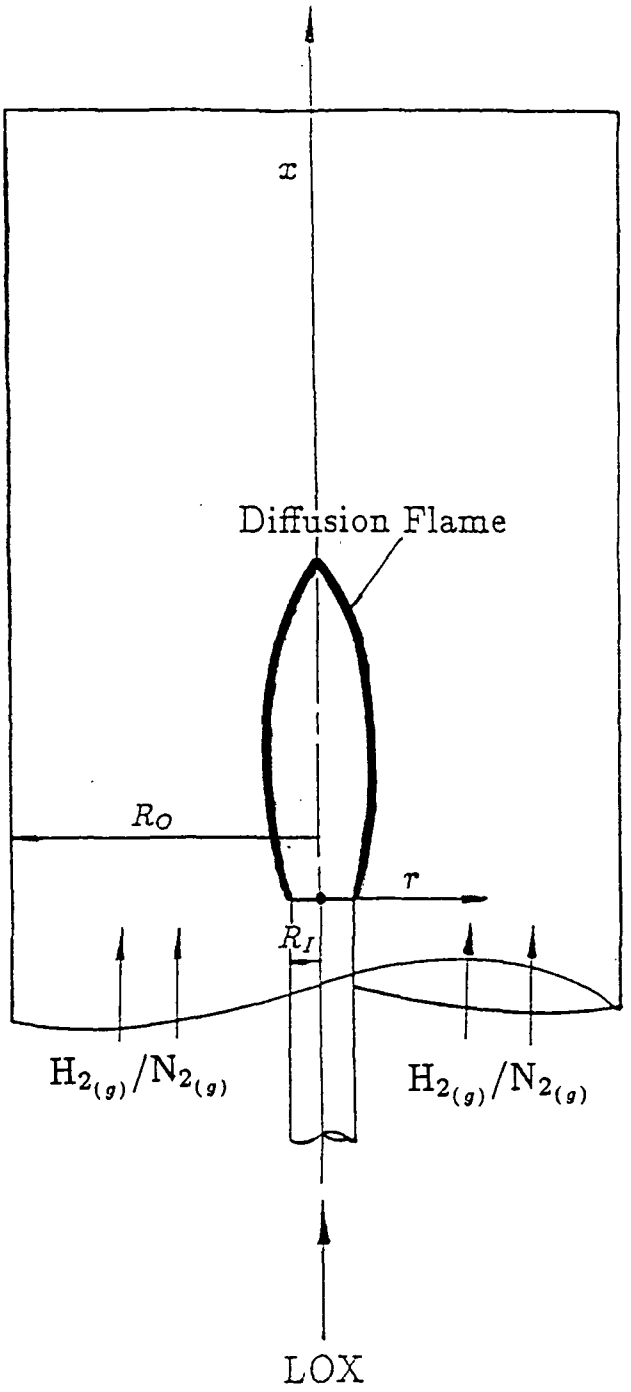

Fig. 1.11 Schematic Diagram of the Combustion of Liquid Oxygen with Gaseous Hydrogen/Nitrogen Mixture

Continuity

$$\frac{\partial}{\partial x}(\rho u) + \frac{\partial}{r\partial r}(\rho r v) = 0 \tag{1}$$

X-Momentum

$$\frac{\partial \rho u u}{\partial x} + \frac{\partial \rho v r u}{r\partial r} = -\frac{\partial P}{\partial x} - \rho g - \frac{2}{3}\frac{\partial}{\partial x}(\mu \nabla \cdot \vec{V}) + \frac{\partial}{\partial x}(2\mu \frac{\partial u}{\partial x}) + \frac{\partial}{r\partial r}(r\mu(\frac{\partial u}{\partial r} + \frac{\partial v}{\partial x})) \tag{2}$$

R-Momentum

$$\frac{\partial \rho u v}{\partial x} + \frac{\partial \rho v r v}{r\partial r} = -\frac{\partial P}{\partial r} - 2\mu\frac{v}{r^2} - \frac{2}{3}\frac{\partial}{\partial r}(\mu \nabla \cdot \vec{V}) + \frac{\partial}{\partial x}(\mu(\frac{\partial u}{\partial r} + \frac{\partial v}{\partial x})) + \frac{\partial}{r\partial r}(2r\mu\frac{\partial v}{\partial r}) \tag{3}$$

where x and r denote the axial and radial coordinates, respectively. The divergence of the velocity vector is given as

$$\nabla \cdot \vec{V} = \frac{\partial u}{\partial x} + \frac{\partial r v}{r\partial r} \tag{4}$$

Energy

$$\frac{\partial \rho u h}{\partial x} + \frac{\partial \rho v r h}{r\partial r} = u\frac{\partial P}{\partial x} + v\frac{\partial P}{\partial r} + \rho\sum_{i=1}^{N} g D_{im}\frac{\partial Y_i}{\partial x} + \frac{\partial}{\partial x}(\frac{\lambda}{C_p}\frac{\partial h}{\partial x}) + \frac{\partial}{r\partial r}(r\frac{\lambda}{C_p}\frac{\partial h}{\partial r}) +$$
$$\frac{\partial}{\partial x}\sum_{i=1}^{N}(\rho D_{im} - \frac{\lambda}{C_p})h_i\frac{\partial Y_i}{\partial x} + \frac{\partial}{r\partial r}\sum_{i=1}^{N} r(\rho D_{im} - \frac{\lambda}{C_p})h_i\frac{\partial Y_i}{\partial r} \tag{5}$$

where h stands for the specific enthalpy of the gas mixture, defined as

$$h = \sum_{i=1}^{N} Y_i h_i = \sum_{i=1}^{N}(h^0_{f,i} + \int_{T_{ref}}^{T} C_{p,i} dT)Y_i \tag{6}$$

The subscript i represents species i and N is the total number of species under consideration.

Species-Concentration

$$\frac{\partial \rho u Y_i}{\partial x} + \frac{\partial \rho v r Y_i}{r \partial r} = \frac{\partial}{\partial x}(\rho D_{im} \frac{\partial Y_i}{\partial x}) + \frac{\partial}{r \partial r}(r \rho D_{im} \frac{\partial Y_i}{\partial r}) + \dot{\omega}_i \qquad (7)$$

where Y_i and $\dot{\omega}_i$ are the mass fraction and rate of production of species i, respectively. For non-reacting flows, the source term in the species transport equation will be zero. In addition, Fick's law is adopted to approximate the species diffusion in the mixture while D_{im} is the effective mass diffusion coefficient for species i.

Equation of State

$$\rho = P/(R_u T \sum_{i=1}^{N} \frac{Y_i}{W_i}) \qquad (8a)$$

The ideal-gas law is adopted to solve the gaseous density. However, near the LOX surface, the temperature of mixture may drop down to 90K. Because the ideal-gas equation may lead to some errors in determining gaseous density at low temperatures, a ninth-order polynomials are employed for density calculations in the 90 - 250K range. Thus, we have

$$\rho = \sum_{n=0}^{9} c_n T^n = c_0 + c_1 T + c_2 T^2 + ... + c_9 T^9 \qquad (8b)$$

And the coefficients c_n are the function of pressure.

3.2 Liquid-Phase Analysis

The liquid-phase analysis is considered to be the one-dimensional flow with uniform bulk motion. Therefore, the physical processes involved are modeled with the energy and species-concentration equations.

Energy

$$\frac{d\rho uh}{dx} = \frac{d}{dx}(\frac{\lambda}{C_p}\frac{dh}{dx}) + \frac{d}{dx}\sum_{i=1}^{N_l}(\rho D_{im} - \frac{\lambda}{C_p})h_i\frac{dY_i}{dx} \tag{9}$$

Species-Concentration

$$\frac{d\rho uY_i}{dx} = \frac{d}{dx}(\rho D_{im}\frac{dY_i}{dx}) \tag{10}$$

3.3 Gas/Liquid Interface Boundary Conditions

The heat and mass transport rate between the gas and liquid phases must be balanced at the interface. conservation laws at the gas/liquid surface, the mass consumption rate and temperature at the interface are determined as follows.

Overall Mass Balance

$$\dot{m}'' = [\rho r_l]_- = [\rho u]_+ \tag{11}$$

Mass Balance for Species i

$$\left[\dot{m}''Y_i - \rho D_{im}\frac{\partial Y_i}{\partial x}\right]_- = \left[\dot{m}''Y_i - \rho D_{im}\frac{\partial Y_i}{\partial x}\right]_+ \tag{12}$$

Energy Balance

$$-\lambda\frac{\partial T}{\partial x}\Big|_- = -\lambda\frac{\partial T}{\partial x}\Big|_+ \quad + \quad \left\{\sum_{i=1}^{N}[\dot{m}''Y_i - \rho D_{im}\frac{\partial Y_i}{\partial x}]_+\right\}\Delta H_{v,i} \tag{13}$$

where r_l and $\dot{m}''$ are the LOX feeding velocity and mass consumption rate per unit surface area, respectively. $\Delta H_{v,i}$ is the specific latent heat for species i. The

subscripts "+" and "−" designate the conditions at the gas and liquid sides of the interface, respectively.

In addition to the above matching conditions, several other boundary conditions are required to close the theoretical model. For the gas phase, we have

Inlet $(x = 0_+)$

$r < R_I$

$$\begin{aligned} u &= u_+ \\ v &= 0 \\ P &= P_+ \\ T &= T_+ \\ Y_i &= Y_{i+} \end{aligned} \tag{14}$$

$R_I < r < R_O$

$$\begin{aligned} u &= u_o \\ v &= 0 \\ P &= P_o \\ T &= T_o \\ Y_i &= Y_{io} \end{aligned} \tag{15}$$

Axis of Symmetry $(r = 0)$

$$\frac{\partial u}{\partial r} = v = \frac{\partial h}{\partial r} = \frac{\partial Y_i}{\partial r} = \frac{\partial P}{\partial r} = \frac{\partial T}{\partial r} = 0 \tag{16}$$

Wall ($r = R_O$)

$$u = v = \frac{\partial h}{\partial r} = \frac{\partial Y_i}{\partial r} = \frac{\partial P}{\partial r} = \frac{\partial T}{\partial r} = 0 \tag{17}$$

Outlet ($x = L_g$)

$$\frac{\partial u}{\partial x} = v = \frac{\partial h}{\partial x} = \frac{\partial Y_i}{\partial x} = \frac{\partial P}{\partial x} = \frac{\partial T}{\partial x} = 0 \tag{18}$$

The boundary conditions for liquid phase are given in the following.

Inflow ($x = -L_l$)

$$\frac{\partial h}{\partial x} = \frac{\partial T}{\partial x} = 0$$

$$Y_{LOX} = 1 \tag{19}$$

Outflow ($x = 0_-$)

$$T = T_-$$

$$Y_i = Y_{i-} \tag{20}$$

3.4 High Pressure Phase Equilibrium

To obtain the species-concentration boundary conditions for each species immediately above and below the liquid surface, the thermodynamic phase equilibrium is imposed upon the gas/liquid interface. At low pressures, the dissolution of ambient gases in the liquid and the influence of pressure on thermophysical properties are negligible. The classical Raoult's law for ideal mixtures, therefore, can well define the phase equilibrium condition. However, in the high pressure environments, fugacity-based multicomponent thermodynamic analysis for vapor-liquid phase equilibrium must be conducted to fully account for ambient gas solubility and real gas effects. The high-pressure vapor-liquid equilibria for each component can be expressed as follows:

$$f_i^{(v)} = f_i^{(l)} \tag{21}$$

$$T^{(v)} = T^{(l)} \tag{22}$$

$$P^{(v)} = P^{(l)} \tag{23}$$

where the superscripts (v) stands for vapor and (l) for liquid. The variable f_i is the fugacity for species i, and can be integrated through the following relation.

$$R_u T \; ln(\frac{f_i}{X_i P}) = \int_{V}^{\infty} \left[\left(\frac{\partial P}{\partial n_i} \right)_{T,V,n_j} - \frac{R_u T}{V} \right] dV - R_u T \; ln Z \tag{24}$$

where X_i and V are mole fraction of species i and total volume, respectively. The above equation indicates that f_i is determined by the properties of the constituent components, the concentrations in both phases, and the temperature and pressure of the system. To compute the integral form in Eq. (24), the Redlich-Kwong (R-K) equation of state is employed.

$$P = \frac{R_u T}{\bar{v} - b} - \frac{a}{\bar{v}(\bar{v} + b)T^{0.5}} \tag{25}$$

where $\bar{v}$ is the molar specific volume. The mixture parameters a, b in cubic-type equation of state can be expressed in terms of composition and pure component parameters.

$$a = \sum_{i=1}^{N}\sum_{j=1}^{N} X_i X_j a_{ij}, \qquad b = \sum_{i=1}^{N} X_i b_i \tag{26}$$

The constants a_{ij}, b_i are essentially dependent on the critical properties of each species. Applying the R-K equation of state and mixing rules to Eq. (24), we have

$$ln f_i = ln X_i + ln P + \frac{b_i}{b}(Z-1) - ln(Z-B) - \frac{A}{B}\left[\frac{2\sum_{j=1}^{N} X_j a_{ij}}{a} - \frac{b_i}{b}\right] ln(1+\frac{B}{Z}) \tag{27}$$

With further manipulations of equation of state, the mixture compressibility factor Z can be solved from the following equation.

$$Z^3 - Z^2 + (A - B - B^2)Z - AB = 0 \tag{28}$$

where

$$A = \frac{aP}{R_u^2 T^{5/2}}, \qquad B = \frac{bP}{R_u T} \tag{29}$$

For a binary system at a given temperature and pressure, Eq. (21) provides two *equilibrium equations. Two more relations can be obtained from the identities:*

$$X_1^{(v)} + X_2^{(v)} = 1, \qquad X_1^{(l)} + X_2^{(l)} = 1 \tag{30}$$

In calculating the mole fractions ($X_1^{(v)}, X_2^{(v)}, X_1^{(l)}$, and $X_2^{(l)}$) of each species, an efficient Newton-Raphson method is used to solve the resulting nonlinear phase equilibrium equations (Eqs. 21 and 30).

Moreover, to accomplish the formation of energy balance at the interface, the heat of vaporization for each species needs to be estimated. By definition,

$$\Delta \bar{H}_{v,i} = \bar{h}_i^{(v)} - \bar{h}_i^{(l)} \tag{31}$$

where the superscript " - " means partial molar quantities. Therefore, $\bar{h}_i^{(v)}$ and $\bar{h}_i^{(l)}$, for example, denote the partial molar enthalpy of the vapor and liquid phases for each species. They both can be calculated from the following thermodynamic relation.

$$\frac{\bar{h}_i^o - \bar{h}_i}{R_u T^2} = \frac{\partial}{\partial T}\left[ln \frac{f_i}{X_i P}\right] \tag{32}$$

where the $\bar{h}_i^o$ designates ideal partial molar enthalpy. Substituting Eq. (27) into Eq. (32) and taking the differentiation with respect to temperature, the latent heat of vaporization can be determined.

3.5 Thermodynamic and Transport Properties Evaluation

In order to simulate various realistic features involved in two-phase evaporation and combustion processes, the pressure and temperature dependence of thermophysical properties must be treated properly. In the present study, the specific heat of each species is determined by a fourth-order polynomial of temperature. Different sets of coefficients, fitted from Sychev et al's (1987) experimental correlations, are used for high-pressure correction. The specific heat of the mixture is acquired by mass fraction weighting of its constituent species. Table 1 outlines the methods for evaluating thermodynamic and transport properties. The specific heat, viscosity, and thermal conductivity are first calculated as functions of temperature and pressure for each constituent species. Subsequently, they are combined together employing suitable mixing or weighting rules. Moreover, for a multicomponent system, the effective diffusion coefficient D_{im} can be expressed in terms of the binary mass diffusivity D_{ij} through the following relationship.

$$D_{im} = (1 - X_i) / \sum_{j \neq i}^{N} \left(\frac{X_j}{D_{ij}} \right) \tag{33}$$

where D_{ij} is calculated adopting Chapman-Enskog theory in conjunction with the Lennard-Jones intermolecular potential-energy functions (Reid et al., 1987). Takahashi's (1974) method is further included to account for high-pressure effect. On the other hand, the liquid-phase mass diffusivity is computed using Wilke and Chang's (1955) approach.

Table 1 Methods for Thermodynamic and Transport Properties Evaluation

Property	Baseline Method[1]	High-Pressure[2] Correction	Mixing Rule[3]
Liquid Density	Hankinson and Thomson (1979)	Thomson et al. (1982)	Hankinson and Thomson (1979)
Gas Specific Heat	Fourth-Order[4] Polynomial of Temperature	Sychev et al. (1987)	Mass Fraction Weighting
Liquid Specific Heat	Sychev et al. (1987)	Sychev et al. (1987)	Mass Fraction Weighting
Gas Viscosity	Lucas (1980)	Lucas (1980)	Lucas (1980)
Gas Thermal Conductivity	Fourth-Order[4] Polynomial of Temperature	–	Mole Fraction Weighting
Liquid Thermal Conductivity	Miller et al. (1976)	Missenard (1970)	Li (1976)
Binary Gas Diffusivity	Chapman and Cowling (1961)	Takahashi (1974)	Fairbanks and Wilke (1950)
Binary Liquid Diffusivity	Wilke and Chang (1955)	–	Fairbanks and Wilke (1950)

1. For pure component at low-to-moderate pressure.
2. For pure component.
3. For mixture.
4. Coefficients of polynomials are fitted from the data of Daubert and Danner (1989) as well as McBride and Zeleznik (1984).

3.6 Gas-Phase Combustion Model

In the consideration of the rate of production of chemical species in the H_2 / O_2 / N_2 system, two different approaches are adopted: (1) an infinitely fast chemistry and (2) a finite-rate chemical reaction mechanism. In the approach of infinitely fast kinetics, chemical reaction rates are assumed to be much faster than the gas-phase mixing rate, and the reactions proceed immediately to completion when the fuel and the oxidizer are mixed at stoichiometric ratio. Solving the transport equations of mixture fraction and the mass fraction of the nitrogen species together with other conservation equations, the distributions of thermodynamic and flow properties are determined. The mass fraction of various chemical species are then computed from their equilibrium relationship with mixture fraction. The flame front location can also be identified.

Although a fast-chemistry model can reasonably well predict several features of the diffusion-flame structure, a finite-rate chemical mechanism has to be resorted if the detailed combustion processes associated with the formation of intermediate species and products are required. Generally, there are two types of schemes could be applied to account for influences of finite-rate chemistry on diffusion flames. One is to employ a whole set of elementary kinetics with known reaction rates. However, due to the inherent complexity of diffusion flames and intensive computation in nature, reduced chemistry with limited rate equations seems to be preferred for practical applications. In this study, a multi-step reaction mechanism will be used to improve understanding of detailed hydrogen/oxygen diffusion-flame characteristics involving the reaction-zone broadening and the existence of nonequilibrium species.

3.7 Numerical Schemes

The conservation equations of mass, momentum, energy and species concentration can be expressed as a generalized vector form as follows.

For the gas phase:

$$\frac{\partial}{\partial x}(\rho u\phi) + \frac{\partial}{r\partial r}(\rho rv\phi) = \frac{\partial}{\partial x}(\Gamma_\phi \frac{\partial \phi}{\partial x}) + \frac{\partial}{r\partial r}(r\Gamma_\phi \frac{\partial \phi}{\partial r}) + S_\phi \tag{34}$$

where

$$\phi = \begin{pmatrix} 1 \\ u \\ v \\ h \\ Y_i \end{pmatrix} \tag{35}$$

$$\Gamma_\phi = \begin{pmatrix} 0 \\ \mu \\ \mu \\ \lambda/C_p \\ \rho D_{im} \end{pmatrix} \tag{36}$$

$$S_\phi = \begin{pmatrix} S_{\phi_1} \\ S_{\phi_2} \\ S_{\phi_3} \\ S_{\phi_4} \\ S_{\phi_5} \end{pmatrix} \tag{37}$$

and

$$\begin{aligned}
S_{\phi_1} &= 0, \\
S_{\phi_2} &= -\frac{\partial P}{\partial x} - \rho g - \frac{2}{3}\frac{\partial}{\partial x}(\mu \nabla \cdot \vec{V}) + \frac{\partial}{\partial x}(\mu \frac{\partial u}{\partial x}) + \frac{\partial}{r\partial r}(r\mu \frac{\partial v}{\partial x}), \\
S_{\phi_3} &= -\frac{\partial P}{\partial r} - 2\mu \frac{v}{r^2} - \frac{2}{3}\frac{\partial}{\partial r}(\mu \nabla \cdot \vec{V}) + \frac{\partial}{\partial x}(\mu \frac{\partial u}{\partial r}) + \frac{\partial}{r\partial r}(r\mu \frac{\partial v}{\partial r}),
\end{aligned}$$

$$S_{\phi_4} = u\frac{\partial P}{\partial x} + v\frac{\partial P}{\partial r} + \rho\sum_{i=1}^{N} gD_{im}\frac{\partial Y_i}{\partial x} + \frac{\partial}{\partial x}\sum_{i=1}^{N}(\rho D_{im} - \frac{\lambda}{C_p})h_i\frac{\partial Y_i}{\partial x} + \frac{\partial}{r\partial r}\sum_{i=1}^{N} r(\rho D_{im} - \frac{\lambda}{C_p})h_i\frac{\partial Y_i}{\partial r}, \tag{38}$$

$$S_{\phi_5} = \dot{\omega}_i.$$

For the liquid phase:

$$\frac{d\rho u\phi}{dx} = \frac{d}{dx}(\Gamma_\phi\frac{d\phi}{dx}) + S_\phi \tag{39}$$

where

$$\phi = \begin{pmatrix} h \\ Y_i \end{pmatrix} \tag{40}$$

$$\Gamma_\phi = \begin{pmatrix} \lambda/C_p \\ \rho D_{im} \end{pmatrix} \tag{41}$$

$$S_\phi = \begin{pmatrix} S_{\phi_1} \\ S_{\phi_2} \end{pmatrix} \tag{42}$$

and

$$S_{\phi_1} = \frac{d}{dx}\sum_{i=1}^{N}(\rho D_{im} - \frac{\lambda}{C_p})h_i\frac{dY_i}{dx}, \tag{43}$$

$$S_{\phi_2} = 0.$$

The afore-mentioned governing equations along with the boundary conditions are solved using the iterative SIMPLE (semi-implicit method for pressure-linked

equations) algorithm (Patankar, 1980). To implement finite control-volume approach, the partial differential equations are first integrated over discrete cells formed by the numerical grids. A set of nonlinear algebraic equations can then be generated. The line-by-line TDMA (tridiagonal matrix algorithm) method is employed to solve the resulting discretization equations for the whole calculation domain. Because of the staggered-grid arrangement, velocity grids are segregated from the scalar grids, and lie right on the surfaces of the control volumes. The power-law scheme is applied to model the both convective and diffusive fluxes across the faces of two finite-difference cells. Futhermore, the harmonic-mean technique for various transport properties at interface between cells is incorporated to accurately represent the diffusion-flux terms over adjacent control volumes. To avoid divergence during the iterations, the underrelaxation is also adopted with a factor of 0.7 for pressure and 0.5 for all other dependent variables.

The calculation starts from an initial guessed conditions over the solving domain except for the boundaries. After performing a number of iterations, corrections of primitive variables are proceeded towards converged solutions. Essentially, each iteration loop comprises the following steps:

1) Guess the values for all flow variables.
2) Evaluate thermodynamic and transport properties from the current conditions of pressure, temperature, and species concentrations.
3) The momentum equations are solved on the basis of guessed pressure distribution to obtain velocity components u and v.
4) Solve the pressure-correction equation derived from the continuity requirement.
5) Correct P and make the corresponding adjustment to the velocity components u and v through the velocity-correction formulas.
6) Solve enthalpy and species-concentration equations sequentially.

7) Specify the corrected pressure P as known and return to step 2).

These steps will be continued until the maximum normalized mass residual has decreased to a required value, which is set as 10^{-6} in this work.

3.8 Overall Solution Procedure

The overall solution sequence uses an iterative technique with interface conditions as convergence criterion. It involves the following procedure:

1) Specify the geometry of computational domain and input all boundary conditions.
2) Set the initial values of surface temperature and LOX feeding rate.
3) Solve the governing equations with the corresponding boundary conditions for both gas and liquid phases.
4) Calculate new surface values of temperature, feeding rate, species concentrations and the latent heat of vaporization through the balance of energy and mass fluxes as well as the high-pressure vapor-liquid equilibria.
5) Check the convergence of surface conditions. If the solution is not converged, return to step 2) with the new surface temperature and feeding rate as the setting values.

The convergence criterion for the above iteration cycle is given as

$$\left| \frac{\phi_s^{(new)} - \phi_s^{(old)}}{\phi_s^{(old)}} \right| \leq 10^{-5} \tag{44}$$

where ϕ_s denotes the surface values of temperature and feeding rate, respectively.

In this study, the finite difference solutions are carried out using 31 $\times$ 23 grids for the gas phase, and 50 grids for the liquid phase. The nonuniform mesh size

is employed, with both axially and transversely clustered grid systems, to resolve steep variations of flow properties near the gas/liquid interface and wall. For each calculation, the conservation of mass flow rate along the axial direction are monitored to be within 0.5%.

4. OVERALL STATUS

The progress made during this reporting period is summarized as follows. Experimentally, a design of the experimental setup and various aspects of safety consideration were planned and implemented. A step-by-step oxygen cleaning procedure for components employed in cryogenic service was developed. The assembly of the apparatus following this strict LOX cleaning procedure has been carried out. In addition, cold-shocked tests of the LOX feeding system have been performed to examine the system integrity. No anomaly was found in these tests. From system check-out tests, a major difficulty in piston leakage was encountered due to the improper function of the spring loaded seal ring. A gas-driven LOX feeding system was then adopted to overcome the leakage problem and demonstrated successful operation by maintaining the LOX surface at the exit of feeding tube. A number of evaporation tests were conducted to justify the assumption of the phase equilibrium at the gas/liquid surface.

Theoretically, a comprehensive model has been formulated and is being solved for studying the evaporation and combustion characteristics of liquid oxygen with hydrogen/nitrogen mixture under subcritical, near critical and supercritical conditions. Important physical and chemical processes are treated in detail. These processes include ambient gas solubility, variable thermophysical properties, vanishing surface tension and latent heat of vaporization at critical mixing point, and chemical kinetics.

REFERENCES OF TASK 1

Chapman, S. and Cowling, T. G. (1961). *The Mathematical Theory of Non-uniform Gases,* Cambridge, New York.

Daubert, T. E. and Danner, R. P. (1989). *Physical and Thermodynamic Properties of Pure Chemicals: Data Compilation,* Hemisphere Publishing Corporation, New York.

Fairbanks, D. F. and Wilke, C. R. (1950). *Industrial and Engineering Chemistry,* **42**, 471.

Hankinson, R. W. and Thomson, G. H. (1979). A New Correlation for saturated Densities of Liquids and Their Mixtures. *AIChE Journal,* **25**, 653.

Li, C. C. (1976). Thermal Conductivity of Liquid Mixtures. *AIChE Journal,* **22** (5), 927.

Lucas, K. (1980). Review of Present Status of Transport Properties Predictions. *Phase Equilibria and Fluid Properties in the Chemical Industry,* Dechema, Frankfurt, pp. 573-587.

McBride, B. J. and Zeleznik, F. J. (1984). Computer Program for Calculation of Complex Chemical Equilibrium Compositions and Applications: Supplement I – Transport Properties. *NASA TM-86885.*

Miller, J. M. Jr., McGinley, J. J. and Yaws, C. L. (1976). Thermal Conductivities of Liquids. *Chemical Engineering,* **83** (23), 133.

Missenard, A. (1970). *Review of General Thermodynamics,* **101** (5), 649.

Patankar, S. V. (1980). *Numerical Heat Transfer and Fluid Flows,* Hemisphere Publishing Corporation, New York.

Reid, R. C., Prausnitz, J. M. and Poling, B. E. (1987). *The Properties of Gases and Liquids,* 4th Ed., McGraw-Hill, New York.

Sychev, V. V., Vasserman, A. A., Kozlov, A. D., Spiridonov, G. A. and Tsymarny, V. A. (1987). *Property Data Update, Official Standards of The National Standard Reference Data Service of the USSR,* Hemisphere Publishing Corporation, Washington D. C.

Takahashi, S. (1974). Preparation of a Generalized Chart for the Diffusion Coefficients of Gases at High Pressures. *Journal of Chemical Engineering* (Japan), **7**, 417.

Thomson, G. H., Brobst, K. R. and Hankinson, R. W. (1982). An Improved Correlation for Densities of Compressed Liquids and Liquid Mixtures. *AIChE Journal,* **28**, 671.

Wilke, C. R. and Chang, P. (1955). Correlation of Diffusion Coefficients in Dilute Solutions. *AIChE Journal,* **1**, 264.

APPENDIX A

OPERATIONAL PROCEDURE FOR LOX/N_2 EVAPORATION TESTS

SETUP

Power Systems

1. Plug the two power strips on the test rig into a shielded extension cable and plug this line into the electric outlet.
2. turn on the two power strips which are mounted on each side of the test setup. This will activate a hydrogen leak detector and provide power to the solenoid valve, the mass flow meters, and four thermocouple readouts.

Gas Supply Systems

- Nitrogen

1. Connect one end of the nitrogen purge line to the low pressure regulator on the nitrogen bottle and the other end to the inlet purge tube.
2. Similarly, connect one end of the nitrogen line to the high pressure regulator and the other end to the nitrogen inlet tube.

- Oxygen

1. Connect one end of the oxygen line to the oxygen bottle pressure regulator and the other end to the oxygen inlet tube located on the test rig. The flow rate of this line can be well adjusted by a micro-metering valve. After introducing gaseous oxygen into the system, the oxygen will be condensed as it passes through the liquid nitrogen bath and enter test chamber as a liquid.

Liquid Supply Systems

Caution: Extreme care must be exercised in use of liquid nitrogen. Due to its cryogenic nature, LN_2 will cause severe burns when in contact with exposed skin. It is recommended that the operator takes the appropriate safety measures, namely, the use of gloves and goggles when handling liquid nitrogen related hardware during the fill operation of the nitrogen bath.

1. Connect the flexible hose to the liquid nitrogen dewar and insert the dispensing end into the nitrogen tank.

Electronic Control/Monitor Systems

1. Calibrate the Validyne pressure transducer and the carrier demodulator that is to be used with it.
2. Connect the demodulator to the pressure transducer and connect the transducer to the test chamber.
3. Connect one end of the BNC cable to the back of demodulator and the other end to the IBM PC/AT computer.
4. Turn on the demodulator.
5. Attach the solenoid control cable to the computer.
6. Turn on the computer.
7. Logon to the pressure control program and perform a function check on the solenoid valve.
8. Turn on oxygen deficiency monitor (should read a value of 20.9).
9. Check hydrogen leak detector (a green light should be activated).
10. Connect each thermocouple to its respective readout if not already connected.
11. Turn on the mass flow meter power supply/readout box.

- Camera

1. Position the video camera in front of the test chamber window.
2. Connect the camera to the VCR recorder and the recorder to a video monitor. The monitor should be visible to an operator standing in front of the control panel.
3. Insert a labeled video cassette into the recorder and turn on the recorder.
4. Turn on the camera and monitor.
5. Set the test information (i.e. title, date, test number, etc) on the picture for future reference. This is done on the camera.

Control Panel

1. Prior to start, open the nitrogen needle valve and leave the hydrogen needle valve closed for evaporation tests.
2. Make sure all pressure gages read zero and thermocouple readouts indicate a realistic room temperature.
3. Close the purge valve.

SETUP CHECKLIST

1. Both power strips are on.
2. Thermocouple readouts are showing data (TCs are working properly).
3. Oxygen and nitrogen lines are securely connected to their inlets on the setup.
4. Liquid nitrogen bath is ready to be prepared.
5. Computer interface is complete; i.e. data lines, BNC cables connected.
6. Demodulator is on.
7. Camera is in position and engaged.
8. Proper needle valve settings on the control panel have been chosen.

TEST PROCEDURE

1. Enter the pressure level to be maintained into the IBM PC/AT pressure control program and initiate the solenoid control sequence. The pressure level is entered as a predetermined demodulator voltage.
2. Briefly open the low pressure nitrogen regulator and purge the oxygen feed line with a pressure of 50 psig.
3. close off the purge valve.
4. Gradually, fill the cooling tank with liquid nitrogen until the liquid reaches a level of 1−2 inches from the top. During this operation the temperature readouts for LOX inlets 1 and 2 should drop to −196.5°C. This provides a means by which to judge whether the oxygen line is submerged by the liquid nitrogen bath.
5. When the nitrogen bath is full, engage the oxygen pressure regulator. Prior to the delivery of gaseous O_2, check regulator to ensure the bottle pressure exceeds that of the chamber pressure by about two times as much.

6. Open oxygen regulator and adjust the pressure until the desired mass flow conditions are met. The micro-metering valve on the test setup should be wide open to accelerate the condensation of O_2 in the feeding tube.
7. Check the high pressure nitrogen regulator to ensure the delivery pressure of the nitrogen exceeds the chamber pressure by about two times.
8. Pressurize the chamber and adjust the mass flow rate of N_2 with the nitrogen needle valve located on the front of the control panel.
9. Turn on the camera and begin recording.
10. When desired chamber pressure is achieved, and liquid oxygen is flowing from the feeding tube, decrease the LOX mass flow by adjusting the micro-metering valve on the oxygen inlet line until the mass flow is minimized. A stable, stationary level of LOX should be maintained at the lowest mass flow rate achievable.
11. Begin data acquisition.

Task No.2
EXPERIMENTAL OBSERVATION OF DENSE SPRAY AND MIXING OF IMPINGING JETS

K. K. Kuo, F. B. Cheung, R. Woodward, M. Kline and R. Burch

The Pennsylvania State University
University Park, Pennsylvania

1. MAIN OBJECTIVE

One of the most important issues to be addressed in the development of advanced liquid rocket engines for space propulsion is how to control the mixing of liquid propellants and eliminate the problem of combustion instability due to inadequate sprays in thrust chambers. Owing to the experimental difficulties in observing dense spray behavior, most of the spray combustion studies performed in the past have focused in the dilute spray region. Very little work has been conducted to explore the characteristics of dense spray. In view of this, an experimental project has been carried out in this task to develop appropriate advanced nonintrusive diagnostic techniques that are suitable for investigating the dynamic interaction between two impinging jets in the near-injector region under both open atmospheric and high pressure conditions. The objective is to visualize the inner jet breakup and mixing processes as well as the outer spray boundary configuration in order to obtain a clear understanding of the physical phenomena controlling spray development from doublet injectors. An effort is also being initiated in this phase of the project to extend the diagnostics studies to the case of spray development from a TRW pintle injector. Based upon the qualitative results obtained in this phase of the project, experimental needs have been identified and methodologies have been developed to determine quantitatively the dense spray behavior of impinging and pintle jets in the subsequent phases. The ultimate goal is to provide the basic information needed to predict the performance of liquid rocket engines and to develop an effective means of enhancing the mixing of liquid propellants as well as to provide the much needed database for model development and validation.

2. Background

Liquid rocket engines over the years have employed a variety of impinging-jet injector designs to mix the fuel and oxidizer. Impinging injector elements may be classified under two categories, unlike- and like-impingement. Unlike elements cause the direct impingement of fuel and oxidizer jets. For like elements, impingement occurs with the same type propellant component to create a spray fan which then mixes with the spray fan of a neighboring element, thus achieving the mixing of fuel and oxidizer. Applications of impinging-element injectors are wide ranging within the liquid rocket field; including the Atlas, Titan III, F-1, LEM Ascent and many small reaction control engines. This type of injector is a common choice for storable liquid propellants. Various combinations of different injector elements may be employed within the same engine for control of both the heat flux to the rocket chamber walls and any resulting non-uniformities in the mixing of the propellants. Generally, the specific injector design is a result of many hours of trial-and-error testing[1]. This is a consequence of the fact that the detailed spray formation processes of impinging-jet injectors are not well defined or characterized with the appropriate controlling parameters such as injector size and geometry, jet velocity, and flow rates. A major motivation for the present work is to seek a better understanding of this important area.

3. Review of Previous Studies

Recently much interest has been renewed in studying impinging liquid jets for rocket engine injector applications. This topic has not been studied in depth since the sixties. The work of Heidmann, Priem, and Humphrey[2] is considered by many to be the definitive work on impinging jet breakup. They characterized four impinging jet flow regimes: the closed rim, periodic drop, open rim, and fully developed regimes. The independent variables considered were jet velocity, surface tension and viscosity. All testing was conducted at open atmospheric conditions.

Heidmann et. al.[2] found that the characteristic spray variation through the four regimes was a strong function of jet velocity or equivalently, the jet Reynolds number. The four spray regimes are described as follows (description applies to area perpendicular to

plane of impinging jets in which a liquid sheet results from the impingement):

1. Closed Rim - At low velocities, a smooth liquid sheet is enclosed by a cylindrical rim which is on the order of the jet diameter.
2. Periodic Drop - As the velocity is increased, small drops begin to shed from this rim, initially near the location of maximum sheet width.
3. Open Rim - At higher velocities, the downstream end of the rim opens, and the sheet disintegrates.
4. Fully Developed - At even higher jet velocities, the spray is described as fully developed when liquid breakup occurs as waves of droplets emanating from the point of impingement.

Although surface tension forces were found to be critical to the transition between flow regimes, variations in surface tension did not change the characteristics of the spray. However, it was observed that higher viscosity fluids produced wider and longer liquid sheets. Changes in jet velocity also affected the sheet length, which asymptotically approached a constant value as velocity was increased. The sheet width was found to be greatest in the open rim regime, decreasing upon transition to the fully developed regime.

Heidmann et. al.[2] observed that in the fully developed regime, the spacing between adjacent waves of droplet formation decreased linearly with jet velocity and also decreased as impingement angle increased (angles from 50° to 100° were tested). Their data also indicated greater dispersion and increased disintegration with increasing impingement angles. Jet diameter was not found to influence the frequency of the waves. Lastly , the data of Heidmann et. al.[2] showed that jet length prior to impingement had negligible effect on wave frequencies, but dispersion increased with jet length.

Dombrowski and Hooper[3] following the work of Heidmann et. al., attempted to clarify which breakup mechanism, i.e. aerodynamic or hydrodynamic (impact) waves, dominated in the disintegration of the liquid sheet formed by the jet impingement. To accomplish this, experiments were conducted with both laminar and turbulent water jets at jet Reynolds numbers to 12,000. Since Heidmann et. al.[2] showed that both jet diameter and

free jet length had little effect on the appearance of the spray, the jet diameter and impingement distance were held constant in this study. Dombrowski and Hooper[3] have shown that waves which apparently originate at the point of impingement and which control the breakdown of the sheet over a wide range of ambient air densities persist even in a vacuum. From this it can be concluded that the waves are not caused by aerodynamic forces but result from the impact of the two jets.

Dombrowski and Hooper's[3] results indicate that these hydrodynamic waves are generated when the Weber number of each jet ($\rho_l DV^2 \sin^2\theta/\sigma$ where ρ_l is the liquid density, D the jet diameter, V the mean jet velocity, σ the surface tension, and θ the impingement angle) is above a critical value, which they concluded to be between 66 and 165 for turbulent jets. They also conclude that the mechanism (aerodynamic verses hydrodynamic) of disintegration of the liquid sheet and resultant drop size are principally dependent on velocity profiles across the jets (independent of Reynolds number) and the angle of impingement. Consequently, for fully-developed turbulent jets with Weber numbers greater than the critical value, impact waves dominate the sheet breakup process over the whole range of operating conditions.

In a report by Bredfeldt[4], a few photographic techniques, such as shadowgraphs illuminated by a collimated spark light source, backlighting techniques through other sources, and the use of the microflash technique of Heidmann et al.[2] are mentioned. A noted deficiency of these techniques occurs in depth of field for focusing the camera, as stated by Bredfeldt, since photographs will absorb all light in the line of sight. Small particles out of focus will appear larger, thus distorting the image, yielding larger drop sizes. In order to resolve this problem angled knife edges were placed in the flow to remove the out of focus portion of the spray. With the current 2-D laser sheet imagery, this depth of field problem is partially eliminated without interfering with the flow, since it offers the ability to distinguish between in and out of focus particles.

As a result of the rejuvenated interest in impinging jet breakup studies, more recent experimental investigations have incorporated laser-based diagnostic techniques, primarily for use in droplet sizing. Studies by Lourme, Schmitt, and Brault[5] and Lourme[6] to characterize the like-on-like doublet injector of the Ariane Viking Engine made use of the

Malvern droplet sizing technique, which is a forward scattering technique based on the principle of Fraunhofer diffraction. These two works focused on obtaining the droplet mass median diameter as a function of injection velocity and orifice geometry. Another important variable considered was that of elevated chamber pressure which was correlated as a gas density effect. The limitation of the Malvern sizing technique concerns droplet concentration. Repeatability and accuracy are guaranteed up to an obscuration value of 0.5, which corresponds to a region of the spray far downstream of the injector exit. However, by using corrective equations calibrated for higher obscuration values of known size distribution, higher droplet concentrations can be analyzed, but in order to provide the drop size distribution in the neighborhood of the injector, another approach is required. In this case, Lourme et. al.[5] and Lourme[6] made use of the "upper mass-flow rate drop size distribution" which is obtained by assuming flow rate conservation for each class of drop size based on distributions experimentally acquired in the dilute spray region.

Another technique studied by Vassallo and Ashgriz[7] is the use of a phase doppler particle analyzer (PDPA) for analysis of the spray. This device, in general, can take measurements in the dilute spray field yielding information on diameter, velocity, number density, and volume flux. However, in the dense spray region, PDPA has severe limitations due to high concentrations of droplets and/or large numbers of non-spherical liquid fragments present in the region of interest.

Since one of the goals of this study is to provide necessary information for impinging-jet spray modeling, the appropriate issues need to be addressed. Spalding[8], in a keynote presentation, identified the needs of computational fluid dynamics (CFD) codes for the modeling of sprays. The difficulties of spray modeling are that there are more than one phase present, surface tension forces present at interfaces, turbulence or random factors present, and the number of quantities needed to characterize the process is large. He identifies additional problems of modeling impinging jet sprays as the determination of the location of the free boundary and the three-dimensional nature of this type of jet. Most other types of jets are axisymmetric about at least one axis.

4. Experimental Method

Two complementary advanced diagnostic techniques are being used to accomplish the previously stated goals: real-time x-ray radiography, which is capable of penetrating the dense spray, and laser-sheet-illuminated photography, which yields high resolution photographs of the spray boundary and droplet regions.

The real-time x-ray radiography system consists of a X-ray source tube, a X-ray image intensifier, a CCD camera, a S-VHS recorder and an advanced digital image processor (see X-ray radiography schematic diagram - Fig. 2.1). A continuous X-ray field is generated by the source tube, which passes through the window of the test chamber and the liquid jets. The X-ray intensity is attenuated by the liquid jets, which contain an X-ray absorber, potassium iodine, KI, in aqueous solution. The X-rays are then converted to fluorescent light and amplified by the X-ray image intensifier. The visible light signal is recorded up by a CCD camera. The X-ray image is processed in real-time by the digital image processor and also recorded by the S-VHS recorder for later playback. This non-intrusive diagnostic technique makes it possible to discern the inner structure of the liquid jet (which is hidden behind optically opaque clouds of liquid fragments) and the void fraction distribution in the dense-spray region.

The experimental setup for the laser-based, 2-D flow visualization technique employed in this study is shown in Fig. 2.2. A 40 W copper-vapor laser supplies ample light for producing extremely short exposure time photographs. The large diameter laser beam (42 mm) is transformed into a thin, parallel sheet of light by an optical system consisting of five beam-steering mirrors, a spherical lens, and two cylindrical lenses. The spherical lens is set up so that its focus is in the center of the region to be photographed. The two cylindrical lenses form a finite sheet of light 39 mm wide and nominally 1 mm thick in the area of interest. If a wider field of view is desired, the sheet is allowed to diverge slightly by moving the second cylindrical lens in relation to the first. A 35 mm SLR camera is placed about a half meter from the injector with the camera axis perpendicular to the light sheet. The light scattered by the impinging jets and resultant spray is collected through a 200 mm telephoto lens with different combinations of a 2X adapter and extension tubes for magnifications up to 7X.

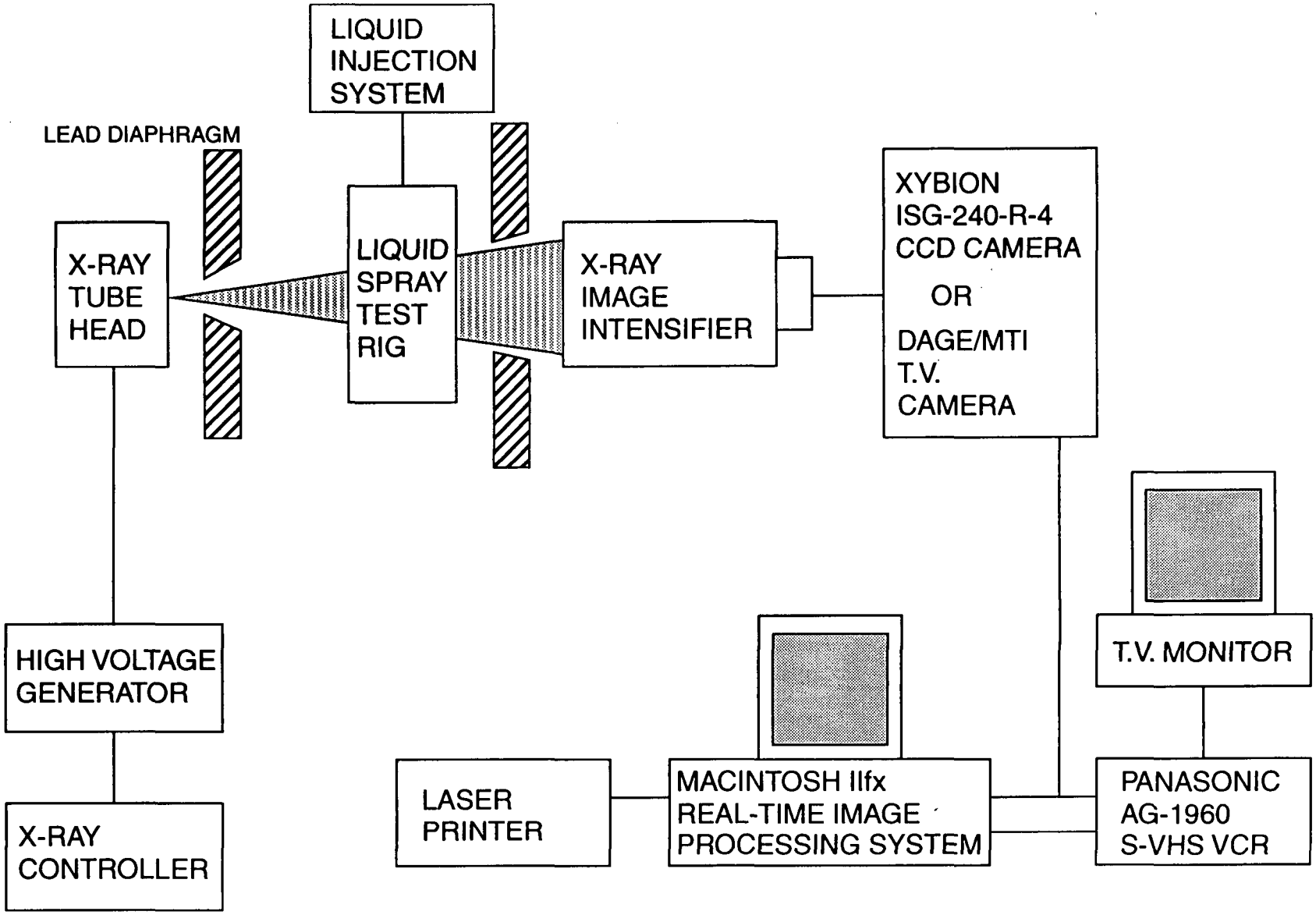

FIGURE 2.1 SCHEMATIC DIAGRAM OF REAL-TIME X-RAY RADOIGRAPHY SETUP

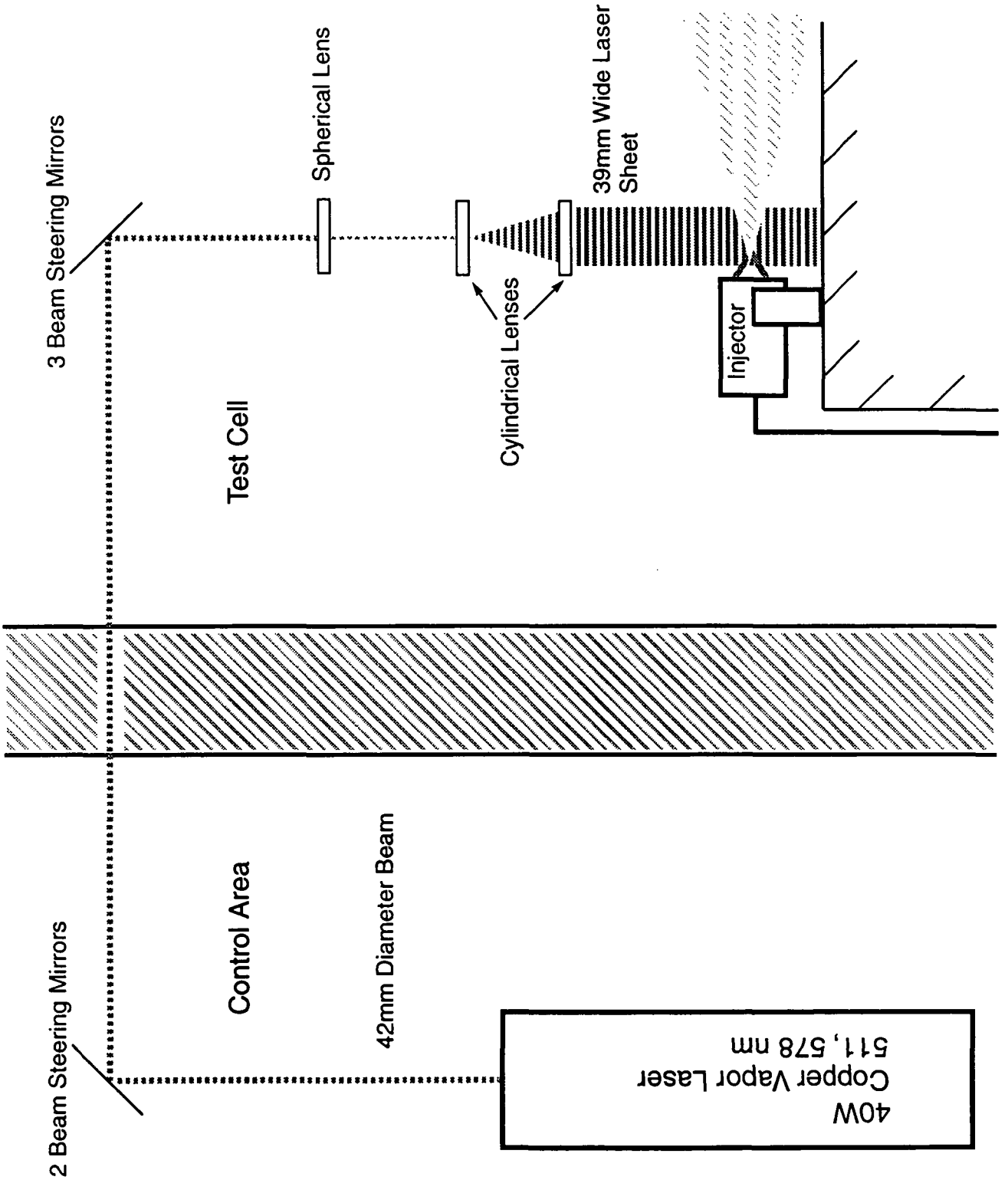

FIGURE 2.2 LASER SHEET PHOTOGRAPHY TEST SETUP

Two different photographic methods are used for extracting complementary information from the spray in the near-injector region. In one method, the camera shutter is held open throughout the test and a single laser pulse of 30 to 60 nanosecond duration exposes the film. This extremely short exposure is capable of completely freezing the liquid motion without streaking to provide an instantaneous view of the spray. The other method essentially creates time-averaged images which are useful to mark the outer boundary of the spray and visualize large scale structures in the flow. In this method, low camera shutter speeds corresponding to exposure times of hundredths to one second are used in conjunction with the laser continuously operating at a pulse frequency of 6.5 KHz. The result is a multiple-exposure photograph consisting of up to thousands of 30 nanosecond exposures.

The injector system consists of a water supply line, a bank of gas bottles for pressurizing with nitrogen, two flow control valves, a liquid supply tank, and an injector assembly. For all cases discussed in this paper, the propellant simulant injected is water. Two injection methods have been employed in the investigation. The first uses tap water directly for low flow rate tests with injector pressure drops to about 0.27 MPa (40 psi). In this case, the liquid supply tank acts as an accumulator in the line. The water flow rate is metered by a hand valve, and the flow is continuous. The second method uses a gas pressurization system to generate much higher liquid supply pressures. Here, the liquid tank is filled and the supply pressure is set at the gas bottles. A remotely actuated ball valve initiates injection. With this injection procedure, injector pressure drops of up to 2.7 MPa (400 psi) have been studied. The major limitation of this method is that with the limited liquid storage capacity of the system (1.3 liter), the test duration is only 3 to 30 seconds depending on the pressure setting.

The injector assembly is of modular design such that different injector configurations can be studied by merely changing the injector faceplate. The study focuses on a like-on-like doublet of the following configuration: 15, 30, 45, 60 and 75 degree total impingement angle, 2.0 mm (5/64 in.) exit diameter, 6.4 length-to-diameter ratio (L/D) of the nozzle passage, and 11.0 mm impingement distance from the injector face. According to the NASA Design Criteria[1] for liquid rocket engine injectors, a nozzle length to diameter ratio of greater than four is recommended for a full flow. NASA Design Criteria[1] also call for an impingement

distance of approximately five to seven diameters. Values greater than ten can magnify jet misalignment. Other injector faceplates have been designed and are awaiting fabrication with the identical L/D and impingement angles, but made out of plexiglas for the visualization of the flow within the orifice. One set of these injectors will be twice the scale to enhance visualization while still preserving the parameters listed above. The modular design of the injector assembly will also allow unlike doublet and triplet configurations to be tested with only slight hardware modifications in the future phases.

The high pressure test rig at the PSU High Pressure Combustion Lab used for the study of coaxial jets at increased back pressure has been modified to conduct impinging jet experiments. Two full length plexiglas windows allow for visualization of the flow by photographic means with the intention of increasing the chamber pressures up to 100 psig. The high pressure test rig is instrumented with thermocouples and pressure transducers to monitor flow rates and chamber test conditions. The injection system for elevated back pressure experiments is shown in Fig. 2.3.

The major parameter currently considered in this investigation is the injection flow rate or, equivalently, the jet velocity. The mean velocity of the impinging liquid jets prior to impingement is deduced from the injection pressure versus time trace. A pressure transducer mounted at the upstream end of the injection assembly, and measurements were recorded via a PC-based data acquisition system. The mean jet velocity was deduced from the known liquid-holding capacity of the system and the test duration taken from the pressure trace. This procedure does not work for the continuous flow tests since they have no real beginning or end. The velocity in such a case was deduced from a correlation of velocity versus injection pressure developed from the aforementioned tests. The specific test pressure history is used whenever possible, and the measurements from each of these tests is continually added to the database supporting the velocity-pressure correlation.

5. Results and Discussion

Multiple sets of 35 mm photographs have been taken for impinging jets at 60° with velocities ranging from 1.5 to 55 m/s (Re_D from 3,000 to 107,000) both in the impingement plane and the plane perpendicular to the impingement plane. The four suggested regimes

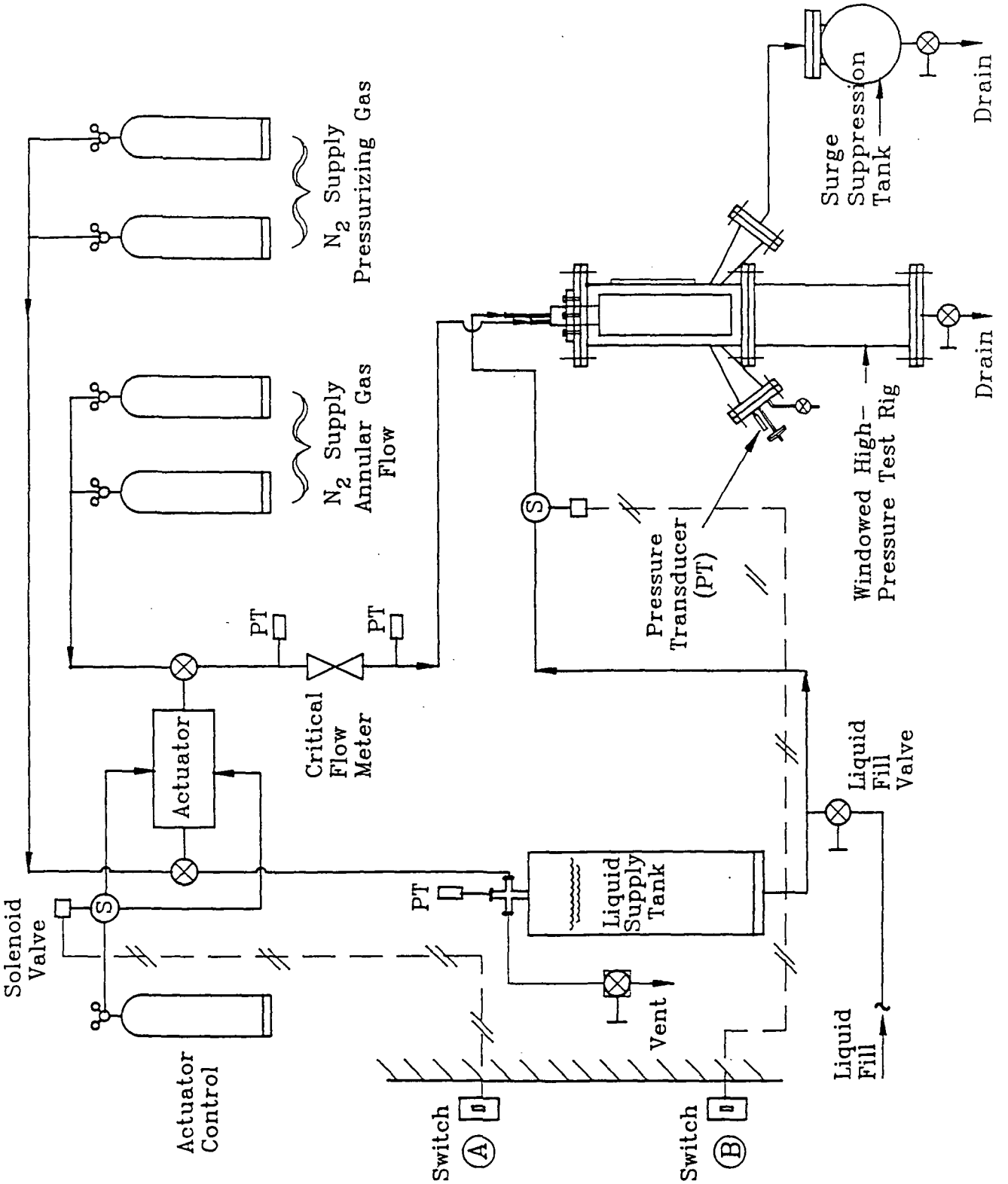

Figure 2.3 High pressure Test Assembly

defined by Heidmann et al.[2] were observed and photographed at velocities ranging from 1.5 m/s for the closed rim up to approximately 12 m/s for the start of the fully developed spray in which waves of droplets and ligaments are visible perpendicular to the plane of impingement with an apparent increase in frequency as the flow rate is increased. However, at velocities above 20 m/s, the wave pattern appears to break down. This suggests the possible existence of an additional regime of breakup beyond the four regimes described by Heidmann et al.[2] Ligaments and droplets that were in concentric waves about the impingement point appear to restructure, eliminating the periodicity. This phenomenon may possibly be caused by the eddy motions which result in strong local turbulent mixing within the spray as well as the generation of fine droplets due to pre- and post-impingement breakup of the jets. The pre-impingement breakup may be due to the separation of the flow in the orifice. This might create a cavitating region which restricts the flow passage in the injector. This would then increase the turbulent nature of the jets as seen by the change of the flow pattern in the resultant spray.

Reproduced in Fig. 2.4 are a series of black and white photographs with both orientations of the injector (with flow from left to right). These photographs show the development of the flow with increasing Reynolds number. The first set of photographs clearly shows the leaf formation in the closed rim regime (3.5 m/s). The rim boundaries are clearly seen. The rim thickness appears to be on the same order as the diameter of the jet. The upper and lower rims are connected by a thin liquid sheet. This liquid sheet is the origin for the wave pattern which breaks down as the velocity is increased. The second set of pictures (4.7 m/s) shows a liquid sheet still intact with relatively large droplets being shed from the rim. The third set of photographs (6.9 m/s) demonstrates the disintegration of the rim boundary on the downstream end. Also, the wave structure appears to be forming from the remains, but with interconnected ligaments. The fourth set, (13.6 m/s), shows the fully developed spray and the waves of droplets and ligaments as described by Heidmann et al.[2] In the fifth set at a velocity of 32.6 m/s, it is evident that atomization has already begun prior to the impingement point. Note that the spray in the plane of impingement does not exceed the total impingement angle at any velocity, whereas the spray perpendicular to this plane clearly diverges with increases in velocity.

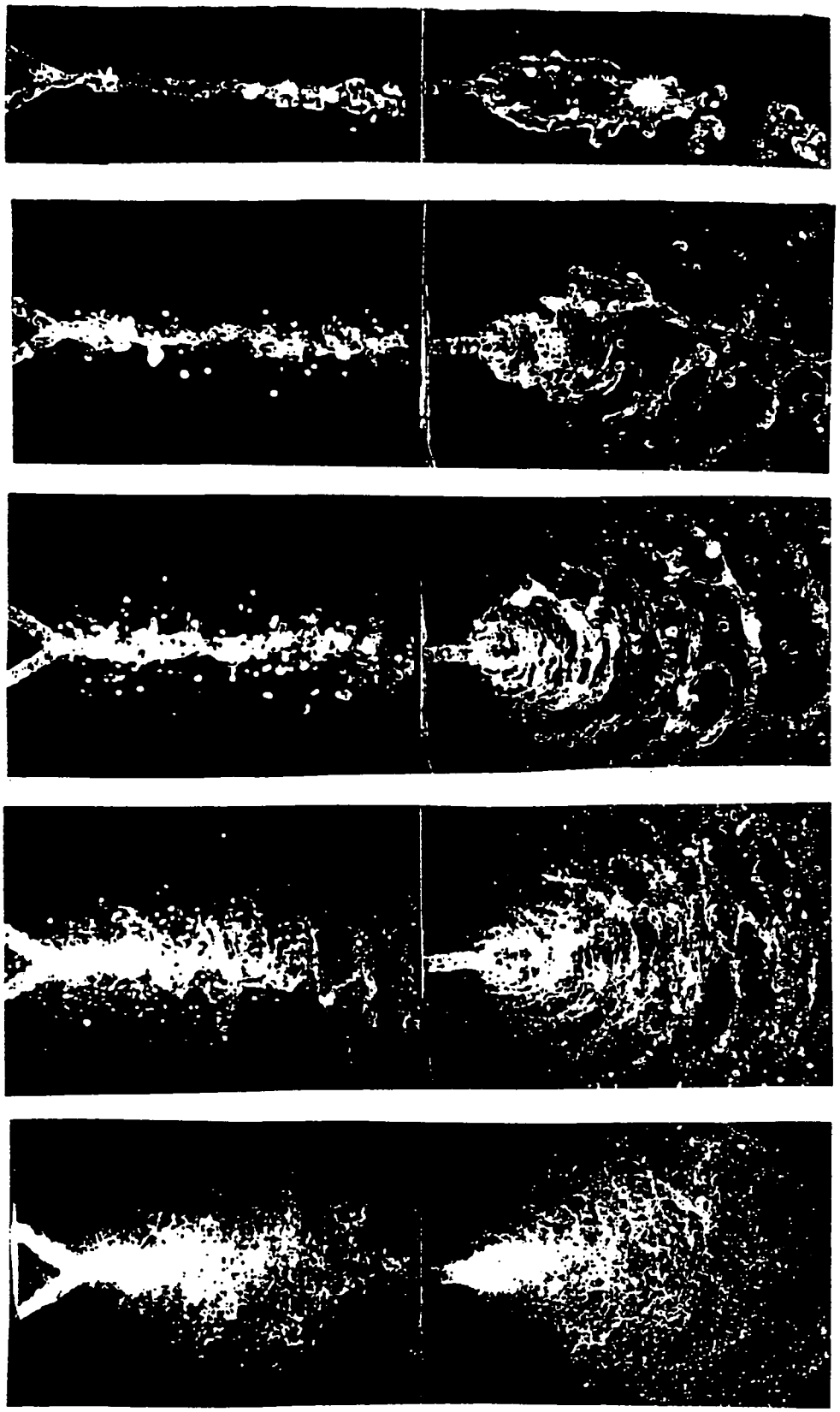

Figure 2.4 Photographs of the impinging jet in the plane of impingement and perpendicular to the impingement plane.

It is evident from the last set of Fig. 2.4 that the resultant spray in this regime is very complex. Obviously, the small scale structure of the flow has become much finer, the cause of which may have been introduced prior to impingement. The occurrence of jet breakup prior to impingement could be largely responsible for the apparent disappearance of the wave pattern in the post-impingement spray. To illustrate the surface wave breakup phenomenon of impinging jets in this regime, a close-up photograph is given in Fig. 2.5. Multiple-scale surface irregularities are evident on the jets in this figure. It is speculated that these surface irregularities imply the existence of fully developed turbulence in the liquid jets. As a result of the pre-impingement jet breakup, the wave structure that would have been formed in the post-impingement region at lower Reynolds numbers is not observed. The result is a flow with multiple characteristic frequencies with the previously well defined breakup frequency, seen in the fourth set of Fig. 2.4, obscured by the small scale motions. Evidence of these fine scales is the apparent increase in number of droplets along with a substantial decrease in drop size. Although the overall spray shape does not change drastically, increases in Reynolds number increase the turbulent intensity, thus enhancing the small scale structure.

Figure 2.6 compares photographs taken perpendicular to the plane of impingement at the same velocities with different angles of impingement. It is clear that as impingement angle increases the spray fan broadens while the apparent length decreases due to jet momentum and surface tension effects.

In Fig. 2.7, a typical set of multiple-exposure pictures are compared to a corresponding set of 30 to 60 nanosecond exposure photographs of the approximate velocity ranges. The multiple-exposure photographs were verified to be statistically stationary at identical conditions. At low velocities, gravity effects are important, bending the downstream end. Note that this flow regime is of little interest for practical propulsion applications. The effect of gravity diminishes as the inertial force (velocity) is increased. While the multiple-exposure photographs yield information on the overall spray shape and trajectories of the droplets, the short exposure pictures provide information on the instantaneous spray pattern.

Using the multiple-exposure pictures, an attempt has been made to correlate the

Figure 2.5 Close-up (enlarged) view of the point of impingement (v=23.5 m/s, Re_D=46,300, angle of impingement=75°).

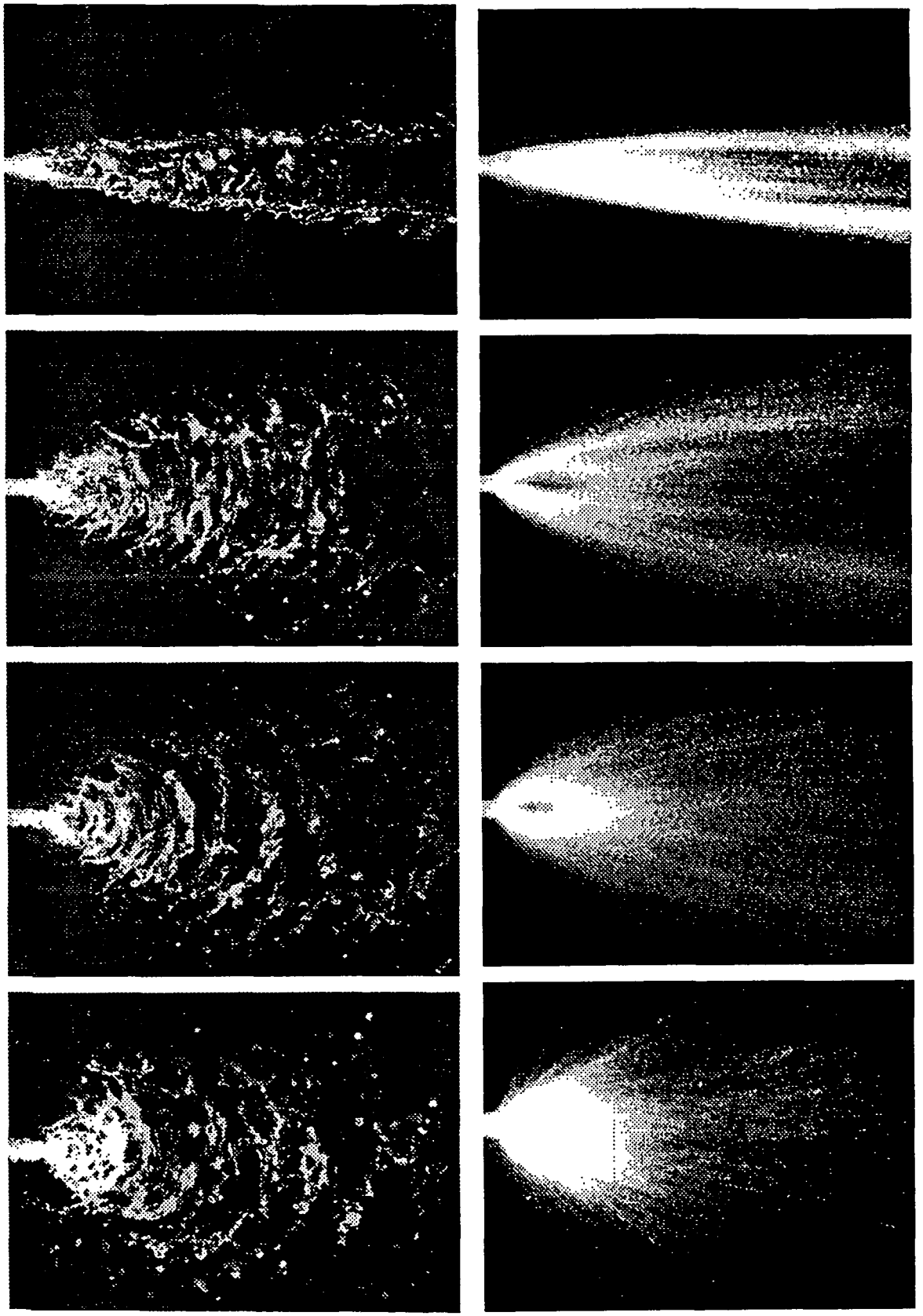

Figure 2.6 Comparison of multiple-exposure (time-averaged) with instantaneous photographs as spray angle increases (ΔP=9.5 psi, v=10 m/s, Re_D=21,370).

v = 2.5 m/s
Re_D = 4,800

v = 3.1 m/s
Re_D = 6,000

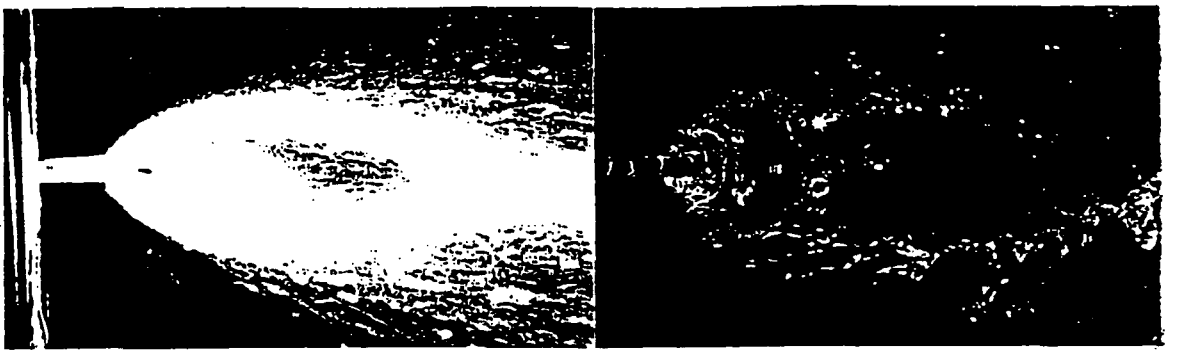

v=4.9 m/s
Re_D=9,700

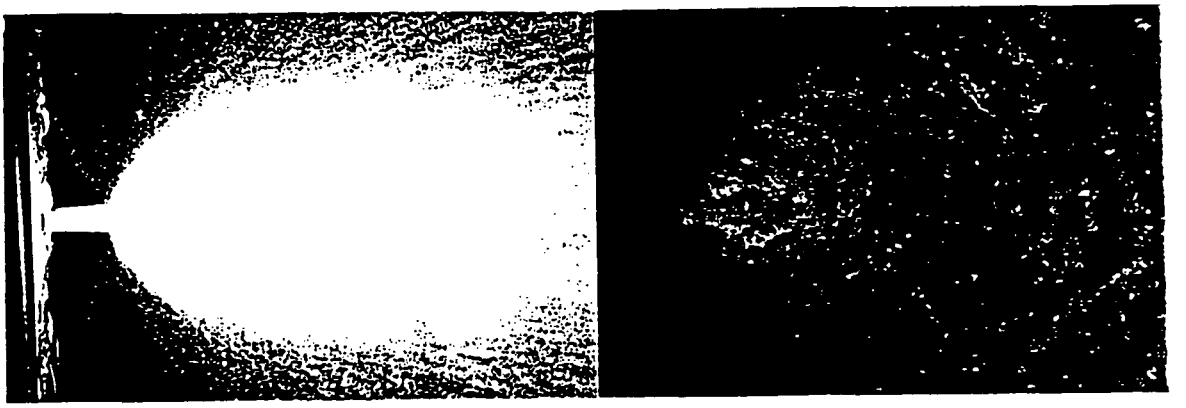

v=12.2 m/s
Re_D=24,000

v = 21.1 m/s
Re_D = 41,500

Figure 2.7 Comparison of multiple-exposure (time-averaged) with instantaneous photographs.

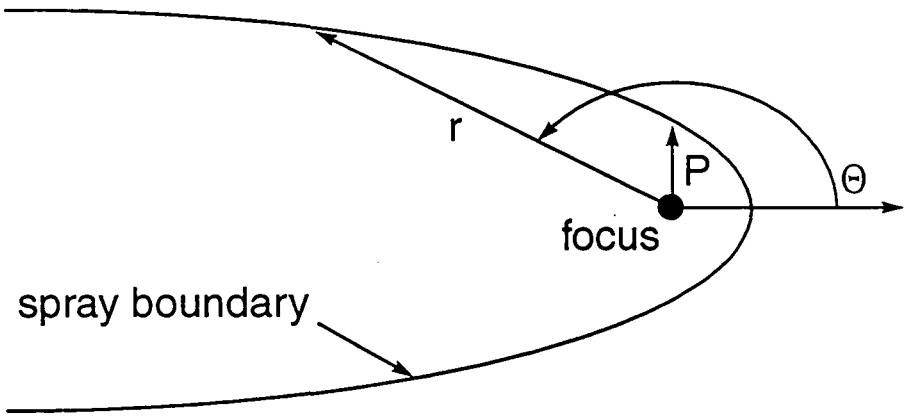

$$r = \frac{P}{1 + e \cos \Theta}$$

r = radius (cm)
P = shape parameter (cm)
e = eccentricity
Θ = polar angle

Figure 2.8 Equation of a conic.

spray shapes to geometric contours of the ellipse, parabola and hyperbola (see Fig. 2.8). From the present study, it is clear that a single spray angle is not sufficient to describe the shape of the spray. The shape parameter, P, sometimes referred to as semi-latus rectum, is determined by fitting a curve to mapped points from the multi-exposure photograph with the focus at the point of impingement. The shape parameter and the eccentricity, e, are varied through use of the polar form of the equation of a conic section. Figure 2.9 shows how the fitted conic section compares to the actual shape of the resulting spray. The outer spray which encompasses nearly all droplets is mapped with a hyperbola and the inner or main spray (which contain the bulk of the liquid in the spray except those on the fringe region) is fitted to a elliptic conic section.

The shape parameter, P, is plotted in Fig. 2.10 versus the jet Reynolds number, Re_D. This graph includes the shape parameter for both the main (inner) and outer spray boundaries. Note that these two curves have the same general shape with the outer spray curve shifted above that of the main spray. The shape parameter increases sharply with increasing Reynolds number up to a value of about 20,000. The shape parameter then decreases slightly in a transition region and gradually recovers to an asymptotic value. The "transition" region may be associated with the transition to fully developed turbulence in the liquid jets. In cases investigated, the pre-impingement jets are clearly experiencing surface breakup at a jet Reynolds number about 30,000. As stated earlier, this preliminary breakup may lead to the disappearance of the well-defined wave pattern observed in the fully developed flow regime described by Heidmann et al.[2]

Preliminary tests of the impinging jet injector in the high pressure test rig have been conducted to observe the effects of increased back pressure on the spray patterns.

Spray boundary data is being analyzed for the injector impingement angles of 15, 30, 45, and 75 degrees. The data is expected to be similar to that obtained from the 60 degree angle measurements. Spray regime maps could then be constructed once the origin of the fifth regime is more clearly understood.

Toward this end, a qualitative study of the possibilities of a detached flow within the orifice (leading to a region of cavitating flow within the injector element) is being conducted presently with a literature search on the subject. This will then be extended to observe the

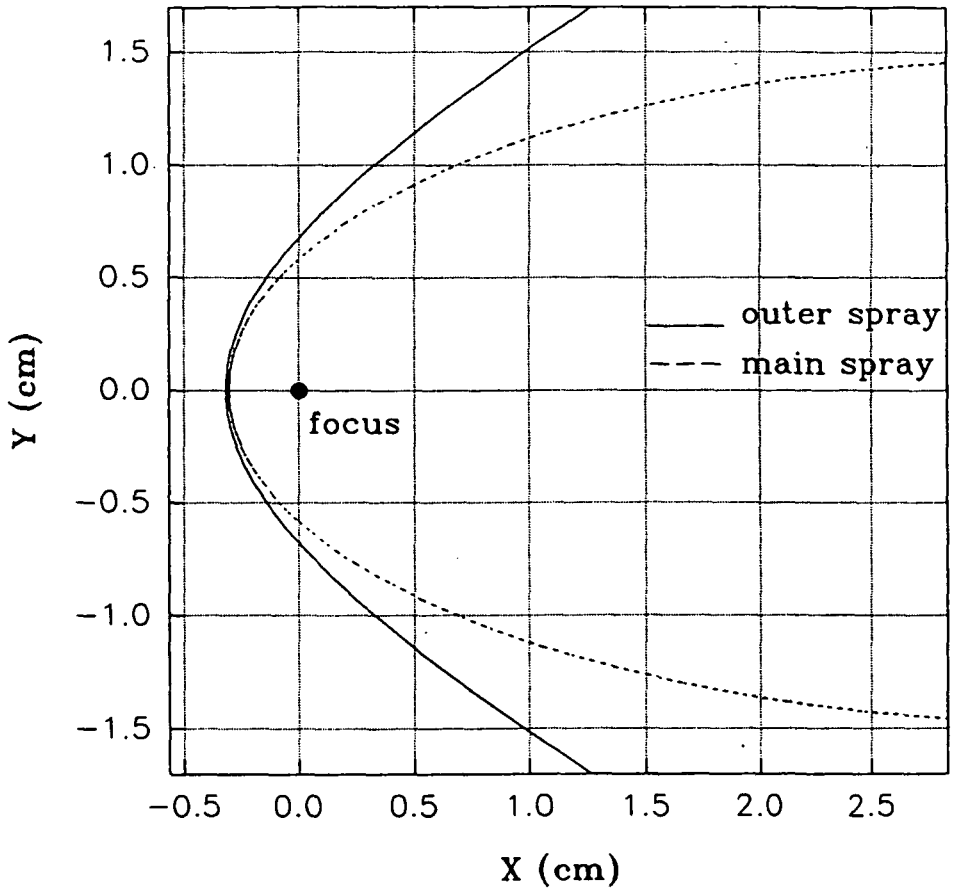

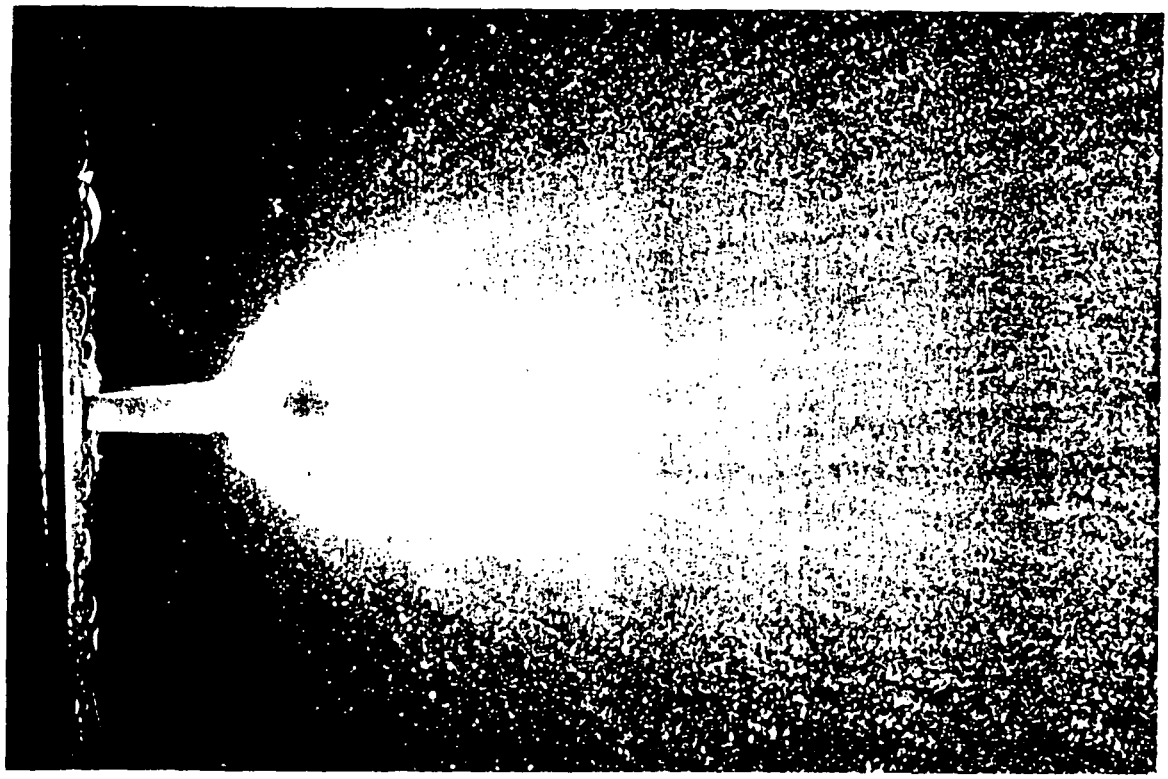

Figure 2.9 Comparison on conic fit to multiple-exposure photograph (v = 12.2 m/s, Re^D - 24,000)

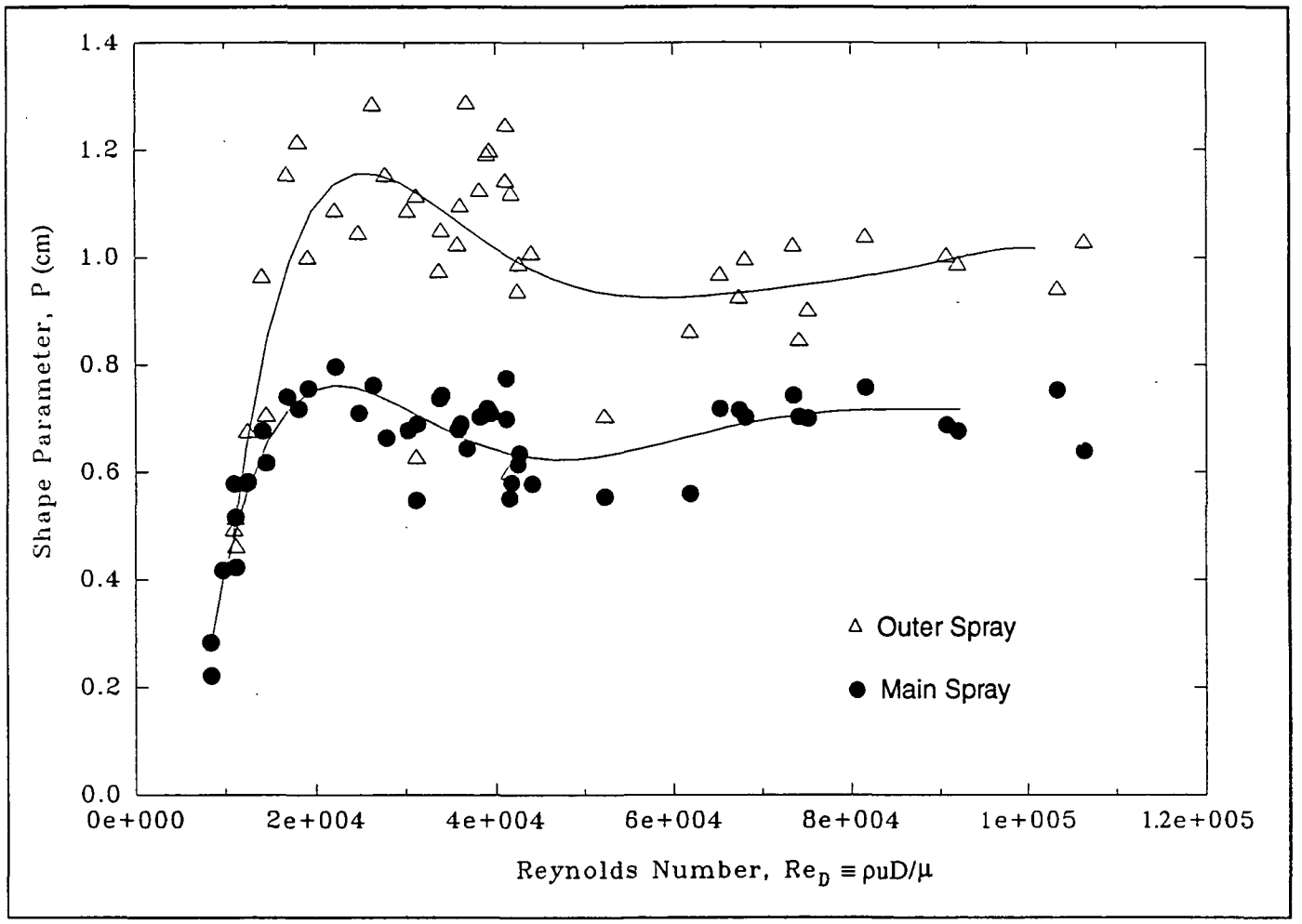

Figure 2.10 Shape parameter vs. Reynolds Number (Total Angle =60 degrees).

flow using the plexiglas injectors and the photographic methods developed.

6. Conclusions

1. The four impinging jet spray regimes (i.e. closed rim, periodic drop, open rim and fully developed spray) originally described by Heidmann et al.[2] have been reviewed and experimentally observed using laser-sheet illuminated photography. In so doing, the data obtained in this investigation suggest the existence of another flow regime beyond their fully developed spray regime. Although the shape or extent of the spray boundary does not change appreciably beyond Heidmann's fully developed regime, the structure of the spray itself under goes a further transition when the jet Reynolds number is beyond a critical value. This transition to much finer temporal and spatial scales results from increased turbulence intensity. The consequence is a loss in the well-defined breakup wave pattern. A qualitative study of this phenomenon did not rule out cavitation in the orifice as the source of increased turbulence.

2. Both short exposure (30 to 60 nanosecond) photographs and multiple-exposure (up to several thousand) photographs were obtained for sprays formed from impinging jets. Short exposure photographs provide detailed instantaneous pictures of the spray contours, while multiple-exposure photographs yield information of a time-averaged images.

3. It is evident from the photographs that the spray sheet widens and the length of the intact liquid sheet decreases as the angle of impingement increases under the same flow conditions. This is believed to be due to the balance between surface tension forces and jet momentum.

4. Traditionally, overall spray development has been described using a spread angle that encompasses the flow. From the photographs presented in this paper, it is clear that the spray resulting from jet impingement does not lend itself very well to such a description, especially when applying a single spread angle to multiple flow regimes. The authors believe that the spray time-averaged boundaries can be well represented in all regimes by one of the conic sections, i.e. ellipse, parabola, or hyperbola, all of which are described by a single equation. The outer spray boundary was found to be characterized by a hyperbolic section while the main boundary by a elliptic or parabolic section.

7. Plans for Future Work

Future work will focus on two major topics: validation of the fifth flow regime, which was described earlier in the paper, and development of the pintle injector test program. The fifth flow regime that occurs during atmospheric testing of the doublet injector needs confirmation of its cause. The question remains: Is the fifth flow regime actually a new flow regime or is it a result of cavitation caused by the injector geometry and the particular testing conditions? An in-depth study should be done in an attempt to identify the existence of cavitation in the orifice and correlate it with the appearance of the new flow regime. The pintle injector test program will take the methods and experience developed in the past and combine them with new ideas to provide an extensive diagnostic study of the spray development from the TRW pintle injector.

The cavitation question should be studied by flow visualization within the injector orifice combined with testing at higher back pressures. The flow visualization within the orifice will confirm the existence of cavitation during the testing. The injector geometry can then be modified to prevent the onset of cavitation such as smoothing the orifice entrance. Conducting tests at higher back pressures will make it impossible for the pressure within the orifice to drop below the vapor pressure of the working fluid thereby making cavitation in the orifice impossible. If the fifth flow regime can be reproduced without the existence of cavitation, there is justification for the existence of a valid flow regime. If not, there will be conclusive evidence that the flow regime is an effect of cavitation within the nozzle.

The pintle injector test program will focus on the flow pattern and the characteristics of the flow. The flow leaving the pintle injector forms an annular cone which breaks up into separate streams at a distance downstream. The investigation will determine the solid angle of the annular cone, the intact sheet length before breakup of the annular cone into separate droplet streams, and the resulting number of streams beyond the intact sheet length. A parametric study of the effects on the shape and breakup of the annular cone due to variations in mass flow rates, surface tensions, viscosities, and densities of the two working fluids flowing through the injector will be performed. The goal is to fully characterize the spray patterns of the TRW pintle injector.

7. References of Task No. 2

1. Anon., NASA Space Vehicle Design Criteria (Chemical Propulsion), "Liquid Rocket Engine Injectors", NASA SP-8089, March 1976, 122 pages.
2. M. F. Heidmann, R. J. Priem, and J. C. Humphrey, "A Study of Sprays Formed by Two Impinging Jets", NACA TN 3835, 1957 (Supersedes NACA TN 2349).
3. N. Dombrowski and P. C. Hooper, "A Study of the Sprays Formed by Impinging Jets in Laminar and Turbulent Flow", J. Fluid Mechanics, Vol. 18, pp. 392-400, 1964.
4. H. R. Bredfeldt, "Evaluation of a Light Scattering Technique for Determining the Spray Characteristics of Impinging Jets", Princeton University, Department of Aerospace and Mechanical Sciences, Technical Report No. 648, 1964.
5. D. Lourme, D. Schmitt, and F. Brault, "Experimental Characterization of the Spray Originating from an Impinging-Jet Injector in a Liquid-Rocket Engine", Acta Astronautica, Vol. 11, No. 7-8, pp. 469-482, 1984.
6. D. Lourme, "Like-on-Like Injector Spray Characterization for the Ariane Viking Engine", AIAA Paper 86-1444, AIAA/ASME/SAE/ASEE 22nd Joint Propulsion Conference, Huntsville, AL, June, 1986.
7. P. Vassallo and N. Ashgriz, "Effects of Flow Rate on the Spray Characteristics of Impinging Water Jets", ICLASS-91, Gaithersburg, MD, July 1991.
8. D. B. Spalding, "Computational Fluid Dynamics and Its Application to Liquid Atomization and Spray Systems", Keynote Lecture, ICLASS-85, April 1985.

U. Ed. ENG 91-79